© 2021. Published by The Company of Biologists Ltd | Journal of Cell Science (2021) 134, jcs258684. doi:10.1242/jcs.258684

RESEARCH ARTICLE

Titin M-line insertion sequence 7 is required for proper cardiac function in mice

Ariane Biquand[1,2], Simone Spinozzi[1,2], Paola Tonino[3], Jérémie Cosette[1], Joshua Strom[3], Zaher Elbeck[4], Ralph Knöll[4,5], Henk Granzier[3], William Lostal[1,2] and Isabelle Richard[1,2,*]

ABSTRACT

Titin is a giant sarcomeric protein that is involved in a large number of functions, with a primary role in skeletal and cardiac sarcomere organization and stiffness. The titin gene (*TTN*) is subject to various alternative splicing events, but in the region that is present at the M-line, the only exon that can be spliced out is Mex5, which encodes for the insertion sequence 7 (is7). Interestingly, in the heart, the majority of titin isoforms are Mex5+, suggesting a cardiac role for is7. Here, we performed comprehensive functional, histological, transcriptomic, microscopic and molecular analyses of a mouse model lacking the *Ttn* Mex5 exon (ΔMex5), and revealed that the absence of the is7 is causative for dilated cardiomyopathy. ΔMex5 mice showed altered cardiac function accompanied by increased fibrosis and ultrastructural alterations. Abnormal expression of excitation–contraction coupling proteins was also observed. The results reported here confirm the importance of the C-terminal region of titin in cardiac function and are the first to suggest a possible relationship between the is7 and excitation–contraction coupling. Finally, these findings give important insights for the identification of new targets in the treatment of titinopathies.

KEY WORDS: Cardiomyopathy, Heart failure, Titin, Mex5, is7, Alternative splicing

INTRODUCTION

Titin is the largest described protein with a molecular mass of 3 to 3.7 MDa, and is the third most abundant protein in striated muscle (Jäckel et al., 1997). A single molecule of titin spans half a sarcomere, from the Z-disc to the M-line, stretching over 1.2 µm (Labeit and Kolmerer, 1995) and interacts with numerous protein partners throughout this length (Chauveau et al., 2014). This giant protein plays a major role in sarcomere stability and organization, and also works as a molecular spring responsible for the passive elasticity of muscle (Gregorio et al., 1998; Granzier and Labeit, 2004). In relation to the sarcomere, titin is organized into four distinct regions that differ in structure and function: the N-terminal segment that anchors titin to the Z-disc through binding to multiple proteins; the I-band, which constitutes the molecular spring region of titin; the A-band region, involved in thick filament length control; and a final C-terminal portion bound to thick filaments in the M-line, where two adjacent titin molecules overlap in an antiparallel orientation (Chauveau et al., 2014; Mártonfalvi et al., 2014).

In humans, the titin gene *TTN* (MIM #188840) is located on chromosome 2q31; it is 294 kb and contains 364 exons (the first non-coding exon plus 363 coding exons), which can theoretically generate over a million splice variants (Bang et al., 2001; Guo et al., 2010). Traditionally, titin isoforms are divided into three main categories depending on presence of the N2A and N2B elements within the I-band region of the protein. N2A isoforms (which contain only N2A elements) are mainly expressed in skeletal muscles, while N2B and N2BA isoforms (which contain only N2B elements, or both N2B and N2A, respectively) are specific to the heart (Linke et al., 1999; Freiburg et al., 2000; Labeit et al., 2006). In addition to this 'splicing hotspot', alternative splicing can also occur in the Z-disc and M-line regions of titin. The latter is encoded by exons 359 to 364, or Mex1 to Mex6. It is composed of a serine/threonine kinase (TK) domain followed by an alternation of immunoglobulin domains (M1 to M10) and unique insertion sequences (is1 to is7) (Fig. 1A). The TK domain is an inactive pseudokinase scaffold and acts as a strain sensor (Puchner et al., 2008; Bogomolovas et al., 2014).

There are numerous binding partners for titin in the M-line region, including M-protein, FHL2 and myomesin 1 (Hu et al., 2015; Lange et al., 2002; van der Ven and Fürst, 1997). Alignment of the M4 domain with myomesin stabilizes the sarcomere during contraction (Lange et al., 2009). In its most terminal region, M10, titin interacts with obscurin (Obscn), obscurin-like 1 (Obsl1), cardiomyopathy-associated protein 5 (Cmya5) and alpha-synemin (Synm) (Fukuzawa et al., 2008; Prudner et al., 2014; Sarparanta et al., 2010). Interestingly, the only exon of this region that can be spliced out is Mex5 (Kolmerer et al., 1996). The fraction of fibres expressing a Mex5+ titin isoform is dependent on the muscle, with a higher Mex5+-to-Mex5− ratio in muscles undergoing aerobic exercises (Guo and Sun, 2018). The splicing of Mex5 exon depends on the species, the phase of development and the M-line structure of the muscle (Kolmerer et al., 1996; Pask et al., 1994). The Mex5 exon encodes for the insertion sequence 7 (is7), situated between two Ig domains, M9 and M10 (Fig. 1A). is7 is part of a binding site for calpain 3, an enzyme implicated in limb girdle muscular dystrophy R1 and which is nearly absent in the heart (Richard et al., 1995; Charton et al., 2010). Fascinatingly, is7+ titin is the major isoform expressed in the heart (Charton et al., 2016; Guo and Sun, 2018).

Considering its huge size, it is not surprising that *TTN* is subject to numerous mutations. About 1% of the general population carries a heterozygous truncating variation in *TTN* with no consequences (Schafer et al., 2017). When pathological, variations in *TTN* are responsible for titinopathies presenting with muscular and/or

[1]Genethon, 91000 Evry, France. [2]Université Paris-Saclay, Univ Evry, Inserm, Généthon, Integrare research unit UMR_S951, 91000 Evry-Courcouronnes, France. [3]Department of Cellular and Molecular Medicine, University of Arizona, Tucson, AZ 85721, USA. [4]Department of Medicine, Integrated Cardio Metabolic Centre (ICMC), Heart and Vascular Theme, Karolinska Institutet, 141 57 Huddinge, Sweden. [5]Bioscience Cardiovascular, Research and Early Development, Cardiovascular, Renal and Metabolism (CVRM), BioPharmaceuticals R&D, AstraZeneca, 431 50 Gothenburg, Sweden.

*Author for correspondence (richard@genethon.fr)

S.S., 0000-0001-8593-5558; I.R., 0000-0002-6505-446X

Handling Editor: John Heath
Received 25 March 2021; Accepted 6 August 2021

Journal of Cell Science

Journal of Cell Science (2021) 134, jcs258684. doi:10.1242/jcs.258684

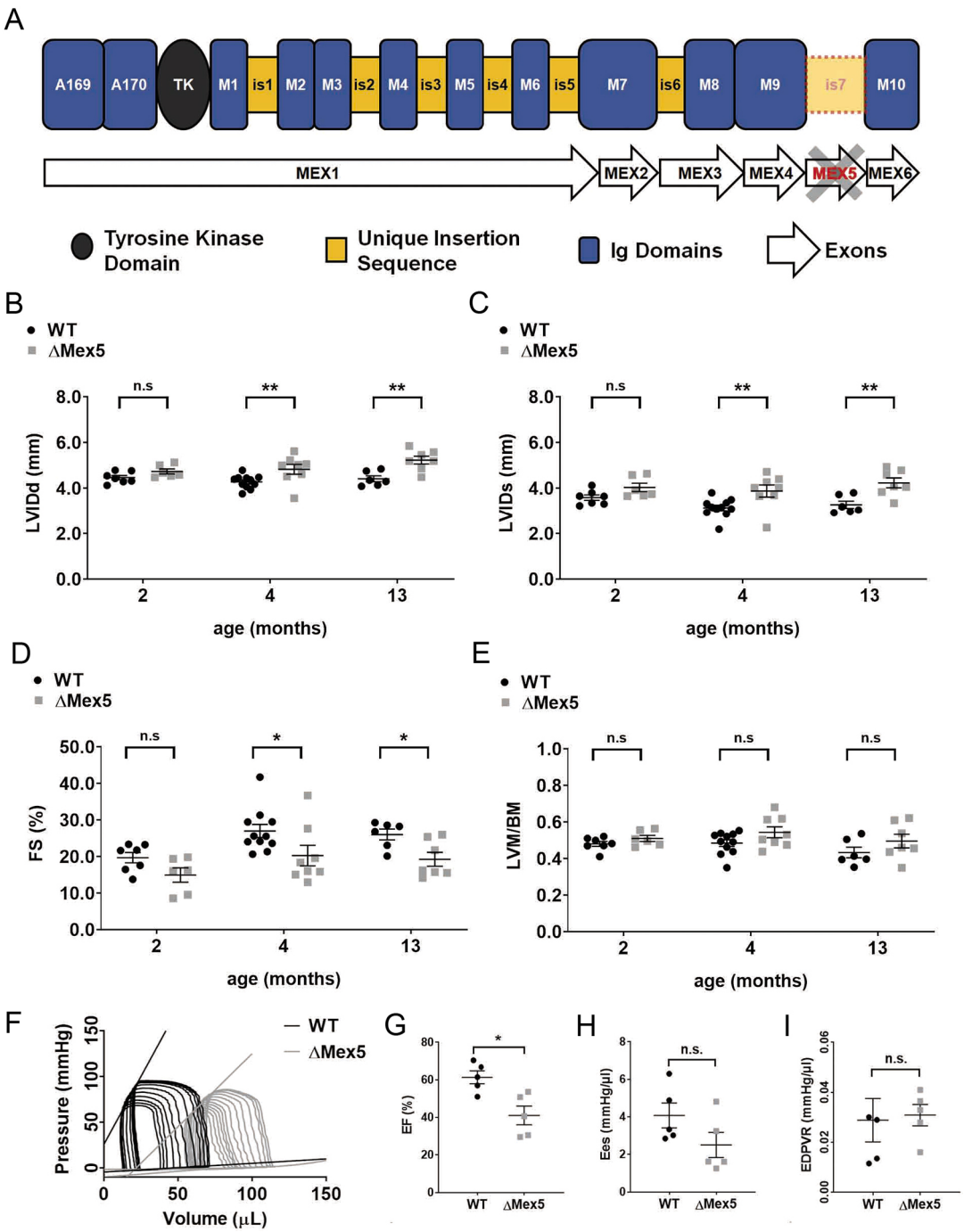

Fig. 1. Cardiac functional characterization of ΔMex5 mice. (A) Schematic representation of titin C-terminal region from exon Mex1 to Mex6, and regions encoded. M, Ig domains; is, unique insertion sequence; Mex, exons. The penultimate Mex5 exon has been deleted in the model. (B–E) Change of LV diameter in diastole (LVIDd), LV diameter in systole (LVIDs), fraction shortening (FS) and LV mass compared to total body mass (LVM/BM) at 2, 4 and 13 months in WT and ΔMex5. (F) Representative PV loops from WT and ΔMex5 mice at 4 months of age. (G–I) Ejection fraction (EF), end-systolic elastance (Ees) and diastolic stiffness coefficient β of EDPVR from WT and ΔMex5 mice at 4 months of age. The mean±s.e.m. is shown. *$P \leq 0.05$; **$P \leq 0.01$; n.s., not significant (unpaired Mann–Whitney test was used to compare groups).

cardiac phenotypes. Titinopathies have highly variable phenotype and prognosis depending on the nature and position of the mutations. Among them, *TTN* mutations are responsible for more than 25% of all dilated cardiomyopathies (DCMs) (Tayal et al., 2017). The majority of reported variants associated with DCM are frameshift-causing mutations in 'high percentage spliced in' (PSI) exons located in the A-band region (Roberts et al., 2015; Stöhr et al., 2018). Animal models also confirmed the importance of several titin regions for the heart function. A canine naturally occurring missense N2B-*TTN* variant in Doberman pinscher dogs leads to DCM and sudden cardiac death (Meurs et al., 2019). Several murine models presenting large *Ttn* deletions have been developed, all presenting with cardiac abnormalities, including homozygous deletion of the PEVK domain (Granzier et al., 2009), of the N2B (Radke et al., 2007), of the N2BA (Nusayr et al., 2018), in the A-band region (Tonino et al., 2017) and in the M-line segment

Journal of Cell Science (2021) 134, jcs258684. doi:10.1242/jcs.258684

(Charton et al., 2016; Gotthardt et al., 2003; Radke et al., 2019). Notably, the M-line region of titin seems to play a determinant role in cardiac function; in fact, the loss of this protein segment is causative of cardiac lethality in mice. The absence of Mex1 and Mex2 exons reduces the mechanical stability of the sarcomere by preventing the formation of a continuous titin filament (Weinert et al., 2006). In cardiomyocytes, the homozygous full deletion of the M-band region abrogates sarcomere formation (Musa et al., 2006). In addition, while mutations in Mex5 are responsible of tibial muscular dystrophies (TMD) in humans (Hackman et al., 2008) deletion of the C-terminal end of titin segment is causative of a myopathy with fatal cardiomyopathy (Carmignac et al., 2007).

Our laboratory previously reported that CRIPSR/Cas9-driven homozygous deletion of the Mex5 exon leads to a dystrophic phenotype of all the muscles that in non-mutant mice mainly express Mex5+ *Ttn* isoforms (Charton et al., 2016). This mouse model (ΔMex5) also showed a progressive cardiac fibrosis, but previous publications were more focused on the skeletal muscle phenotype or the role of the is7 region in the interaction with calpain 3 (Charton et al., 2016; Lostal et al., 2019). Here, we further characterized the cardiac phenotype in ΔMex5 mice, showing that absence of the titin is7 region leads to DCM with decreased cardiac function, also confirming the presence of a progressive fibrosis. Our data showed sarcomere alterations and mislocalization of the C-terminal end of titin in ΔMex5 cardiomyocytes. In addition, molecular analyses revealed that the deletion of is7 caused a decreased expression of the M10-binding partners Obscn and Cmya5. A decreased expression of the two most important excitation–contraction coupling proteins [cardiac ryanodine (Ryr2) and dihydropyridine receptors (Dhpr; also known as CACNA1C)] was also observed. Altogether, these results explain how the deletion of the is7 region is responsible for the appearance of the cardiomyopathy in ΔMex5 mice, by destabilizing the sarcomeric organization in cardiomyocytes, which also suggests a possible alteration of the Ca^{2+} release machinery. To our knowledge, the results reported here are the first demonstration of the potential molecular mechanisms underlying DCM resulting from Mex5 alterations, providing useful insights for future therapeutic targets.

RESULTS

Mex5 homozygous deletion leads to DCM with altered cardiac function and fibrosis in mice

To gain a better understanding of the is7 role in titin function, we previously generated a mouse model homozygous for a deletion of the Mex5 region (ΔMex5) (Fig. 1A) (Charton et al., 2016). The ΔMex5 mice were reported to show a dystrophic phenotype in the skeletal muscle, with the soleus being the most affected muscle and with an involvement of the heart as observed by the presence of fibrotic tissue (Charton et al., 2016). To better understand the role of is7 within the titin molecule, we studied the consequences of its deletion in the heart. Of note, the cardiac tissue is the only muscle where titin isoforms containing this domain are expressed by the majority of the cells, suggesting the particular importance of is7 in this organ.

To evaluate whether the absence of the is7 impacts cardiac function, transthoracic echocardiographic measurements on wild-type (WT) and ΔMex5 mice were performed at 2, 4 and 13 months of age (Fig. 1B–E; Table S1). Echocardiography in ΔMex5 mice showed a progressive increase in the left ventricular diameter in both diastole and systole compared to WT controls, with significant differences starting from four months of age (Fig. 1B,C; Table S1). The change in left ventricular volume is not associated with significant differences in wall thickness, or in the heart weight-to-body weight ratio (Table S1). Chamber diameter abnormalities were accompanied by decreased cardiac function, as shown by reduction in the fractional shortening percentage (Fig. 1D,E; Table S1).

In view of the significantly reduced fractional shortening of the left ventricular chamber in ΔMex5 mice starting at 4 months of age, we assessed systolic and diastolic ventricular properties via pressure-volume (PV) analysis at this time point. PV loops showed (Fig. 1F; Table S2) that, compared to WT mice, the end systolic pressure volume relationship (ESPVR) of the ΔMex5 mice left ventricle (LV) chamber was shifted rightward, as a consequence of the increase in end systolic and end diastolic volumes (Table S2). Although it did not reach a statistical significance, the end-systolic elastance (Ees), which provides an index of myocardial contractility, tended to be decreased in ΔMex5 mice (Fig. 1H) as did the maximal left ventricular pressure (dP/dt max; mmHg/s) (Table S2). The end diastolic pressure volume relationship (EDPVR) and the relative coefficient β, which describes the passive properties of the myocardium, remain unchanged (Fig. 1I). In agreement with echography data, the ejection fraction (EF) was also significantly decreased in ΔMex5 hearts (Fig. 1G; Table S2). Overall, the PV analysis revealed a decreasing trend in cardiac inotropy in ΔMex5 mice, as shown by the reduced Ees, consistent with the ventricular dilatation and dysfunction, but no with change in diastolic stiffness, since no alterations in the coefficient-β were present.

To establish the impact of the Mex5 deletion on heart morphology, light sheet imaging, a technique that allows three-dimensional visualization of organs, was performed on hearts from 4-month-old mice. Longitudinal, sagittal and transversal sections confirmed the left ventricular dilation in ΔMex5 hearts (Fig. 2A). Three-dimensional imaging allowed for a deeper analysis of the heart dimensions that, in contrast with the echocardiography measurements, revealed an observable difference in the LV free-wall between mutant and controls. The light sheet image quantification showed an increase in the volume of all the heart chambers ,also confirming the LV dilation observed in echocardiography (Fig. 2B,C).

Histological and molecular characterizations of ΔMex5 and control hearts were performed at the same time point. Heart tissue sections from 4-month-old mice were stained with hematoxylin phloxin saffron (HPS) and Sirius Red (Fig. 2D). HPS-stained cross-sections of ΔMex5 hearts displayed large areas of damaged tissue with increased cellularity when compared to WT. Sirius Red staining showed an extended presence of fibrotic tissue in ΔMex5 hearts, whereas normal connective tissue was found in WT hearts (Fig. 2D). Additional analyses, at different time points, indicated that the fibrotic tissue was already present in ΔMex5 hearts at 1 month of age (albeit with no significant increase in respect of WT controls), and that the fibrotic condition proportionally worsened with aging (Fig. 2E; Fig. S1A). Immunofluorescence analyses of collagens 1a1 and 3a1 (Fig. S1B) and quantitative RT-PCR analysis of fibrosis markers (collagen 1a1, fibronectin, collagen 3a1 and vimentin) (Fig. 2F,G; Fig. S1C,D) confirmed the observed fibrotic phenotype.

The level of different cardiac stress and inflammation markers that were known to be associated with pathological cardiac conditions, were also measured by quantitative RT-PCR (Fig. 2H–J; Fig. S1E,F). In particular, the balance between the mRNAs encoding for the two myosin heavy chains Myh7 and Myh6 was altered in ΔMex5 hearts, as already reported during pathological heart remodeling (Fatkin et al., 2000; Gupta, 2007; Vanderheyden et al., 2008; Montgomery et al., 2011). The level of *Myh7* was increased, whereas *Myh6* was decreased with respect to WT controls (Fig. 2H,I). Natriuretic peptide A (*Nppa*), whose expression is reactivated in cardiovascular pathologies (Houweling

Journal of Cell Science (2021) 134, jcs258684. doi:10.1242/jcs.258684

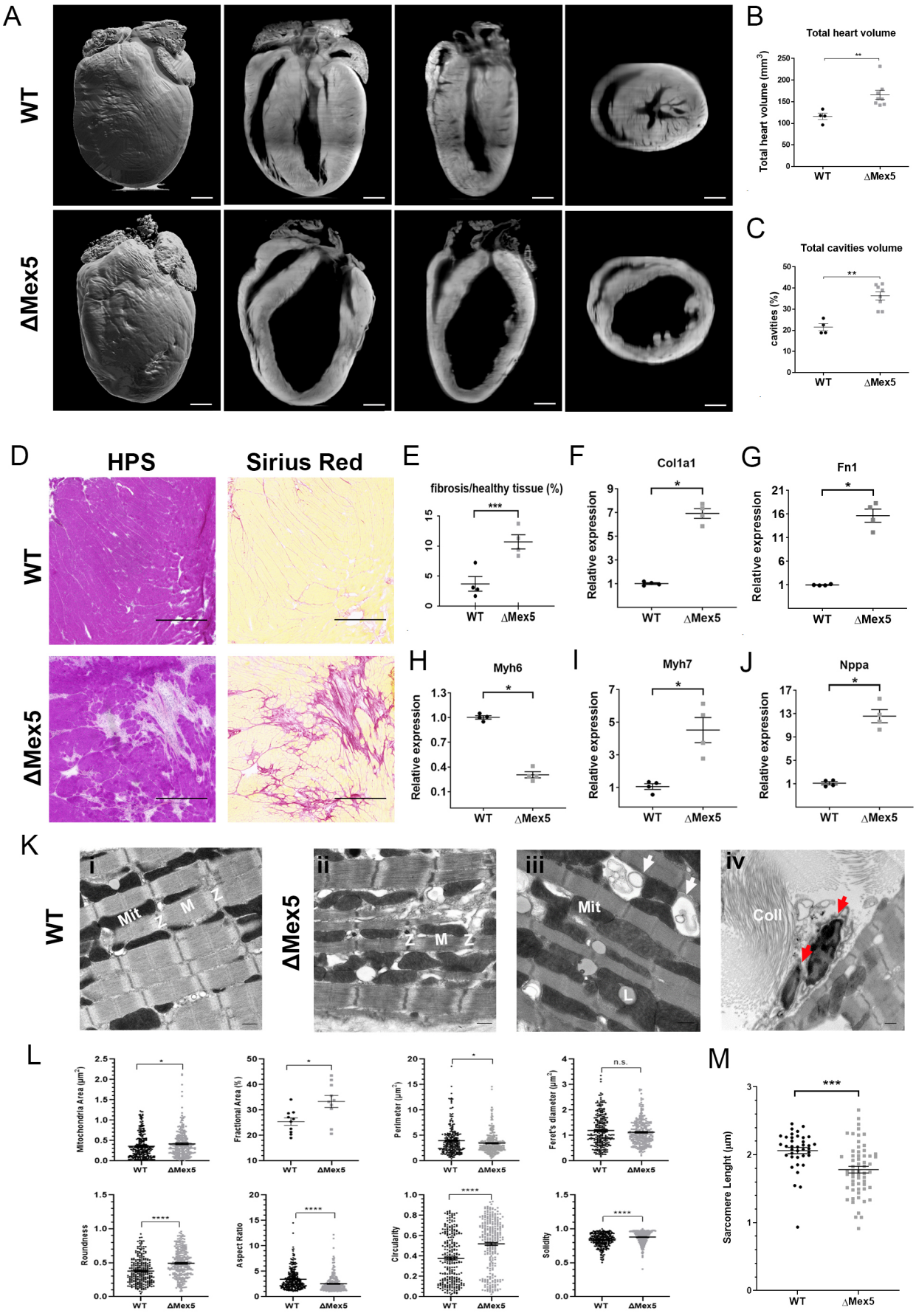

Fig. 2. See next page for legend.

Journal of Cell Science (2021) 134, jcs258684. doi:10.1242/jcs.258684

Fig. 2. Cardiac structural characterization of ΔMex5 mice.
(A) Representative light sheet imaging images from eight repeats of hearts from 4-month-old mice; from left to right: three-dimensional, longitudinal, sagittal, or transversal view. Scale bars: 1 mm. (B) Quantification of the total heart volume. (C) Quantification of the total cavities volume. (D) Histological sections of heart from WT and ΔMex5 mice at 4 months of age stained with HPS and Sirius Red. Scale bars: 10 µm. (E) Sirius Red staining quantification at 4 months of age. Amount of staining is quantified as the percentage of the total tissue section (mean±s.e.m.). (F–J) qRT-PCR results (mean±s.e.m.) for fibrosis and heart damage makers (*Col1a1*, *Nppa*, *Myh7* and *Myh6*) relative expression in WT (set at 1) and ΔMex5 mice hearts at 4 months of age. (K) Representative longitudinal electron microscopy images from four samples of papillary muscle from WT (i) and ΔMex5 (ii–iv) mice at 4 months of age. Irregular Z-disc (Z) and M-line (M) (ii), abnormal condensed mitochondria (Mit), autophagic vacuoles (white arrows), lipids (L) (iii), inflammatory infiltrate cells (red arrows) and collagen fibrils (Coll) (iv). Scale bars: 500 nm. (L) Mitochondria quantitative analyses: area, fractional area, perimeter, Feret's diameter, roundness, aspect ratio, circularity and solidity. Values are expressed as the mean±s.e.m. (WT: n=270 and ΔMex5: n=285 measurements). (M) Sarcomere length measurement (mean±s.e.m.)., *$P\leq0.05$; **$P\leq0.01$; ***$P\leq0.001$; ****$P\leq0.0001$; n.s., not significant (unpaired Mann–Whitney test was used to compare groups).

et al., 2005), transforming growth factor β1 (*Tgfb1*), a key player in cardiac fibrosis and pathological remodeling (Dobaczewski et al., 2011; Hanna and Frangogiannis, 2019) and TIMP metallopeptidase inhibitor 1 (*Timp1*), which is known to be upregulated in deteriorating heart failure (Takawale et al., 2017; Heymans et al., 2005), were all upregulated, indicating a typical DCM pattern in the mutant mice (Fig. 2J; Fig. S1E,F).

To identify the impact of the is7 deletion on sarcomere organization, electron microscopy on heart samples from 4-month-old mice was performed (Fig. 2K). Ultrastructural analysis of ΔMex5 mice cardiac tissue revealed the presence of altered sarcomeres with irregular Z-discs, less defined A- and I-bands, and absence or disruption of the M-line, although occasional normal sarcomere structures were found (Fig. 2Ki,ii). Abnormal condensed mitochondria (Mit), autophagic vacuoles, lipids, inflammatory infiltrate cells and collagen fibrils were also observed, further confirming the fibrotic condition (Fig. 2Kiii,iv). Mitochondria quantitative analyses showed a statistically significant increased area and fractional area, and reduced perimeter in ΔMex5 mice, while no significant differences in Feret's diameter was found (Fig. 2L, top row). Shape parameters were significantly different in ΔMex5 mitochondria compared to WT, including the increase in roundness accompanied by the reduction of aspect ratio, and an increase in circularity and solidity, indicating a reduction in the elongation of ΔMex5 mitochondria (Fig. 2L, bottom row).

We then compared ΔMex5 sarcomere length to WT controls. A huge variation in ΔMex5 sarcomere length was observed compared to controls, with a higher number of shorter sarcomeres in ΔMex5 hearts (Fig. 2M). These data demonstrate that the homozygous deletion of Mex5 in titin is causative of a DCM phenotype accompanied by cardiac fibrosis, inflammation and mitochondria morphological alterations, as well as altered sarcomere length.

Sarcomere alterations and titin 'ultra-localization shift' in ΔMex5 hearts

To investigate the underlying mechanisms leading to the cardiac abnormalities, a first characterization of the consequences of the Mex5 deletion on the expression of titin at the RNA and protein levels was performed. Quantitative RT-PCR showed a slight (albeit not significant) reduction in *Ttn* relative expression in ΔMex5 with respect to WT controls, suggesting that the deletion does not drastically affect *Ttn* mRNA level (Fig. 3A). At the protein level, Coomassie Blue staining of gels loaded with lysates from WT controls and ΔMex5 hearts and subjected to agarose gel electrophoresis was performed to visualize the presence of the different titin isoforms. The results showed no increase in the degradation product T2 in ΔMex5 heart samples compared to controls; a slight decrease in N2BA-to-N2B ratio was observed, although this was not statistically significant (Fig. S2A,B). A more detailed analysis was conducted via western blotting using a set of antibodies raised against all different domains from the C-terminus of titin (M1, is5, is6, M8M9, is7 and M10), while using an antibody specific for the titin N-terminus (Z1Z2) as a comparative control (Fig. 3B). No differences in the amounts of Z1Z2, M1, is5 and is6 were observed between ΔMex5 and WT controls, indicating that the protein is present at similar levels with or without the is7. As expected, no specific labeling was detected for is7 on ΔMex5, confirming the deletion. Interestingly, a reduction of intensity was also observed for the two adjacent domains M8M9 and M10 in ΔMex5 compared to controls, suggesting that the deletion of the is7 affects the adjacent titin Ig domains (Fig. 3C).

Immunostainings of cardiac tissue from 4-month-old mice were then performed to determine the presence of the different domains at the C-terminus of titin and to assess the localization of titin in ΔMex5 mice (Fig. 3D). Is7-specific staining showed the complete loss of the domain, whereas M8M9 and M10 staining confirmed the presence of these domains on each side of the Mex5 deletion in WT tissues, although not all ΔMex5 sarcomeres were positive for M8M9 and M10 staining. Despite a reduced intensity of the staining on WB, immunofluorescence images showed a correct integration of titin in ΔMex5 cardiomyocytes, and no apparent change in localization with respect to WT controls (Fig. 3D).

Immunoelectron microscopy was performed with antibodies raised against is7 and M8M9. As expected, titin is7 was completely absent in ΔMex5 but present in WT sarcomeres, while titin M8M9 domain epitopes were labeled in a spotty pattern in both mutants and controls (Fig. 3E). However, the M8M9 staining was not present in all the sarcomeres and the pattern was less regular in ΔMex5 samples. Measurement of the distance between M8M9 epitopes across the M-line was increased in ΔMex5 compared to WT (88 ±1 nm versus 94±3 nm; mean±s.e.m.), indicating a modification in the organization of the domains and suggesting that the mutation alters titin localization at a sarcomeric level, shifting it more toward the Z-disc side (Fig. 3F).

These results suggest that the absence of $Mex5^{+}$ titin in the heart causes sarcomere abnormalities.

Deletion of is7 leads to a classical molecular signature of a DCM

To understand the molecular mechanisms underlying the cardiac phenotype in ΔMex5 mice, a RNA-seq analysis on samples from WT and mutant hearts at 4 months of age was performed using Illumina sequencing. The reads were aligned onto the mm10 mouse genome and DESeq2 analysis was performed. A total of 3473 genes were identified as significantly dysregulated with a log2 fold change higher than 0.5 in ΔMex5 hearts compared to controls, with 2116 upregulated and 1356 downregulated genes (Fig. 4A). The top dysregulated genes at four months of age sorted by log2 fold change are presented in Tables S3 and S4. These included transcripts encoding for proteins implicated in cardiac fibrotic processes (e.g. Spp1, Cilp, Ltbp2, Sfrp2 and Thbs4), fibrotic tissue structure (e.g. Tnc, Col12a1 and Col8a2) and cardiac protection upon stress (e.g. Mpeg1 and Gpnmb) for the upregulated, and

Journal of Cell Science (2021) 134, jcs258684. doi:10.1242/jcs.258684

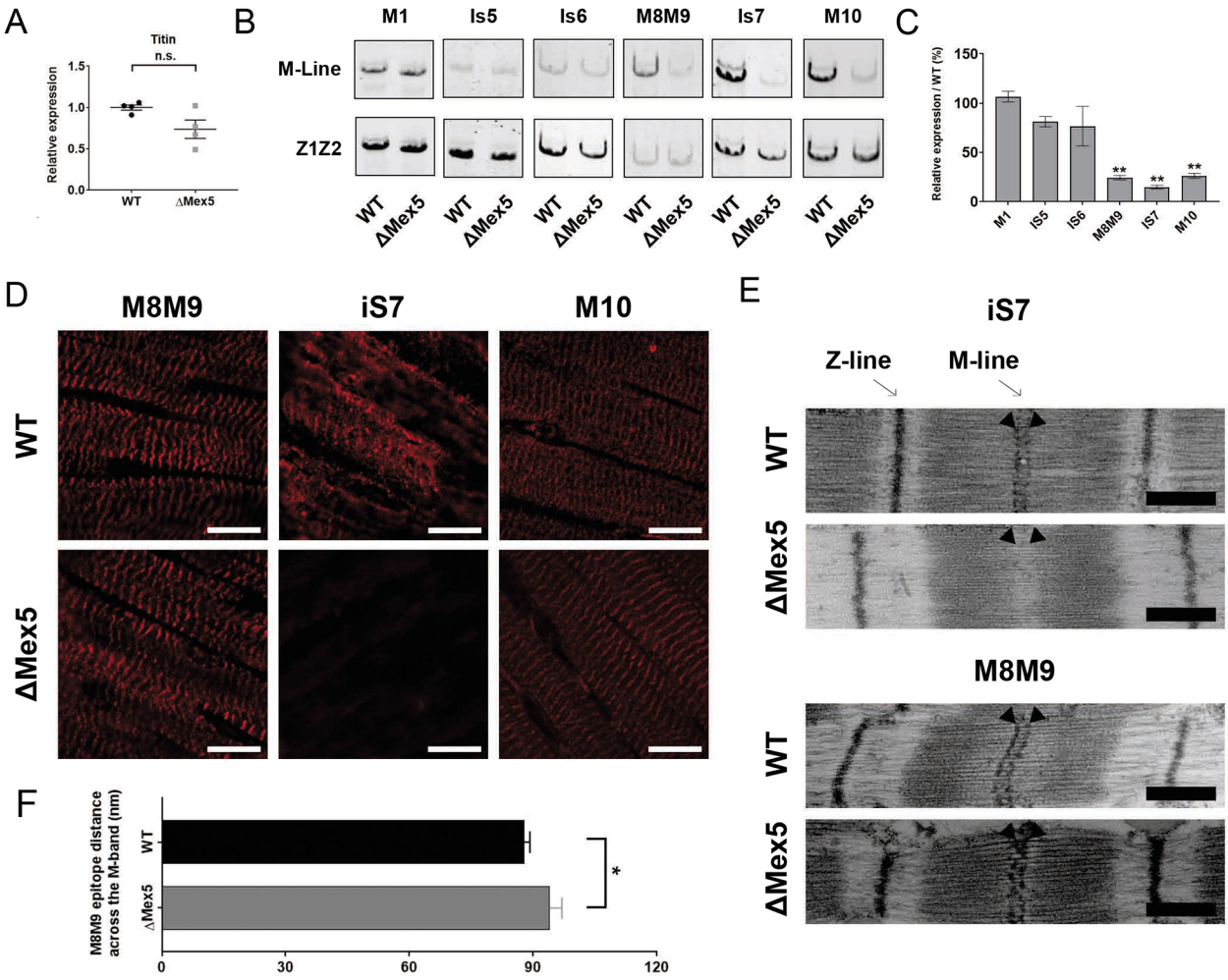

Fig. 3. Sarcomeric characterization of ΔMex5 mice. (A) qRT-PCR results (mean±s.e.m.) for titin relative expression in WT and ΔMex5 mice hearts at 4 months of age. (B) Western blot analysis of full-length Titin terminal domains on cardiac samples from WT and ΔMex5 mice at 4 months of age. Z1Z2, which is situated at the N-terminal region of titin, is used for normalization. The full-length titin predicted molecular mass is ∼3700 kDa. (C) Quantification of the western blot analysis for titin M-line domains normalized to Z1Z2. Relative expression of ΔMex5 to WT is shown (%). (D) M-line immunostaining in WT and ΔMex5 mice hearts samples at 4 months of age using anti-M8M9, -is7 and -M10 antibodies. Images are representative of four experiments. Scale bars: 5 µm. (E) Example of sarcomeres from WT and ΔMex5 mice heart at 4 months of age labeled with titin is7 and M8M9 antibodies (black arrowheads) by immunoelectron microscopy. Scale bars: 500 nm. (F) M8M9 domain epitopes distance across the M-line (mean±s.e.m.) corrected for shrinkage with A-band. *$P \leq 0.05$, **$P \leq 0.01$; n.s., not significant (unpaired Mann–Whitney test was used to compare groups).

in mitochondria for the downregulated (e.g. mt-Ts1 and mt-Ti). Gene Set Enrichment Analysis (GSEA) using the Gene Ontology (GO) Biological Process collection revealed that the most upregulated genes were related to immune response activation (e.g. GO terms leukocyte migration, regulation of cell activation, leukocyte differentiation and adaptive immune response) (Fig. 4B,C; Tables S5, S6). The GSEA also confirmed that the downregulated genes were significantly enriched in the GO terms related to mitochondrial pathways (e.g. GO terms mitochondrial respiratory chain complex assembly, respiratory electron transport chain, mitochondrial electron transport NADH to ubiquinone) (Fig. 4B,D; Tables S5, S6). Ingenuity Pathway Analysis (IPA) software was used to identify enriched pathways. We used the IPA toxicology analysis to obtain a picture of the negative effects of the is7 removal. Most of the significantly dysregulated genes are implicated in known cardiac diseases pathways, such as cardiac enlargement (86 genes), cardiac dysfunction (45 genes), cardiac dilatation (38 genes), cardiac fibrosis (27 genes), cardiac necrosis/cell death (35 genes), etc. (Fig. 4E). These results confirmed that deletion of Mex5 in titin is causative of DCM associated with severe inflammation, cardiac fibrosis and mitochondrial damage.

Interestingly, two genes, *Cmya5* and *Obscn*, encoding for proteins that bind to titin at the M10 region were present among the downregulated group with a high significance (adjusted *P*-values of 4.04×10^{-4} and 0.001, respectively), although were not among the most dysregulated genes (Table S7) (Benian and Mayans, 2015; Sarparanta et al., 2010) . A close homolog of *Obscn* (i.e. *Obsl1*) was also slightly dysregulated (adjusted *P*-value of 0.028). On the other hand, the levels of the two other proteins known to interact with titin in M10, α-synemin (Synm) and calpain 3 (Capn3), which are present at a low expression level, remained unchanged (Table S7). *Cmya5* encodes for the cardiomyopathy-associated protein 5, a 500 kDa tripartite motif (TRIM)-related protein, which is highly expressed in striated muscles and serves as an anchoring protein that mediates subcellular compartmentation of intracellular signaling (Benson et al., 2004, 2017; Sarparanta, 2008). Obscn is a 720 kDa sarcomeric protein with an essential structural role in positioning the longitudinal sarcoplasmic reticulum (SR) at the M-line (Lange et al., 2009). We

Journal of Cell Science (2021) 134, jcs258684. doi:10.1242/jcs.258684

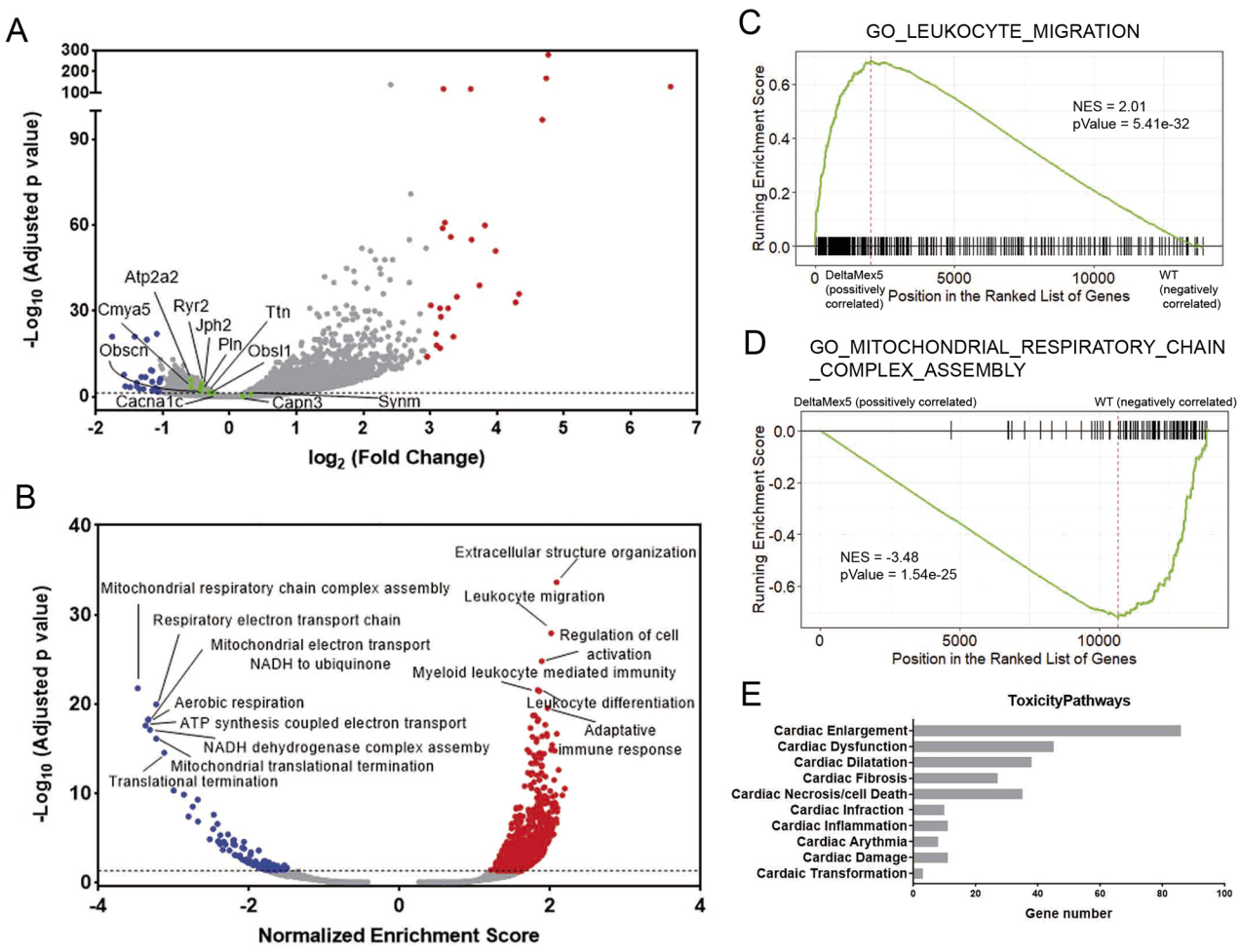

Fig. 4. RNA-seq analysis of ΔMex5 heart. (A) Volcano plot representation of RNA-seq analysis of ΔMex5 mice versus WT hearts at 4 months of age. Red dots, 25 most upregulated genes; blue dots, 25 most downregulated genes; green dots, genes of interest. (B) Volcano plot representation of Gene Set Enrichment Analysis (GSEA) of GO biological processes (blue is a decrease; red is an increase). (C,D) GSEA enrichment score curves of GO term leukocyte migration and GO term mitochondrial respiratory chain complex assembly. (E) Toxicity functions significantly activated in the heart of the ΔMex5 model.

also noticed that two genes, *Ryr2* and *Atp2a2* encoding for Ryr2 and SERCA2, two proteins known to play a central role in Ca^{2+} handling, were downregulated with high significance (adjusted *P*-values 2.5×10^{-5} and 1.6×10^{-6}, respectively; Table S8). RyR2 and SERCA2, are two of the main components of the cardiac $Ca2^{+}$-release/uptake machinery present at the level of the SR, and alterations in their expression levels are a hallmark of cardiac disease (Liu et al., 2019, 2020). Interestingly, Ryr2 clustering in striated muscle involves Cmya5, and these two proteins form an oligomeric protein complex in cardiac muscle (Benson et al., 2017). Genes encoding for two additional proteins involved in Ca^{2+} handling were also slightly dysregulated, namely *Jph2* and *Pln* (Table S8). *Jph2* encodes for junctophilin2, which is a protein determinant in dyad formation between junctional SR and T-tubules (Takeshima et al., 2000; Spinozzi et al., 2020; Feng et al., 2020). *Pln* encodes for phospholamban, a protein that is involved in SERCA2 regulation (Koss et al., 1997).

Deletion of the is7 alters the expression of titin M10-binding partners and of junctional membrane complex proteins in ΔMex5 mice

The data obtained with the RNA-seq analysis guided us in further investigating the dysregulations in titin M10-binding partners and in assessing whether the Ca^{2+}-release and -uptake machinery was altered in the ΔMex5 mice. In agreement with RNA-seq results, quantitative RT-PCR measurements showed a reduced mRNA expression for *Cmya5*, *Obscn*, *RyR2*, *Atp2a2* and *Pln*, whereas *Synm*, *Cacna1c* (encoding for Dhpr) and *Jph2* levels were not significantly changed (Figs 5A–H and 4A; Table S8). At the protein level, western blotting analyses showed a decreased expression only for Cmya5, Obscn and Ryr2 in ΔMex5 mice, in agreement with the reduction at the transcription level (Fig. 5I–L). On the other hand, no significant change in Jph2 or Serca2 was detected between mutant and WT hearts (Fig. 5M,N). Surprisingly, Dhpr protein levels were significantly reduced in ΔMex5 hearts, in contrast with transcriptomic and quantitative RT-PCR data (Fig. 5O). These results suggested a specific alteration in Ca^{2+} release, with abnormal expression of the two main proteins involved in this process, but no apparent alteration in the organization of the junctional membrane complex architecture (no change in Jph2 expression) or in the Ca^{2+}-uptake machinery (no alterations in Serca2 protein levels were observed). Next, we investigated whether Cmya5 and/or Obscn localization was impacted by the destabilization of the M-line portion of titin in mutant mice. Immunofluorescence analyses on heart sections from 4-month-old ΔMex5 and WT mice showed no altered pattern for either Cmya5 or Obscn in mutant mice. α-Actinin

Journal of Cell Science (2021) 134, jcs258684. doi:10.1242/jcs.258684

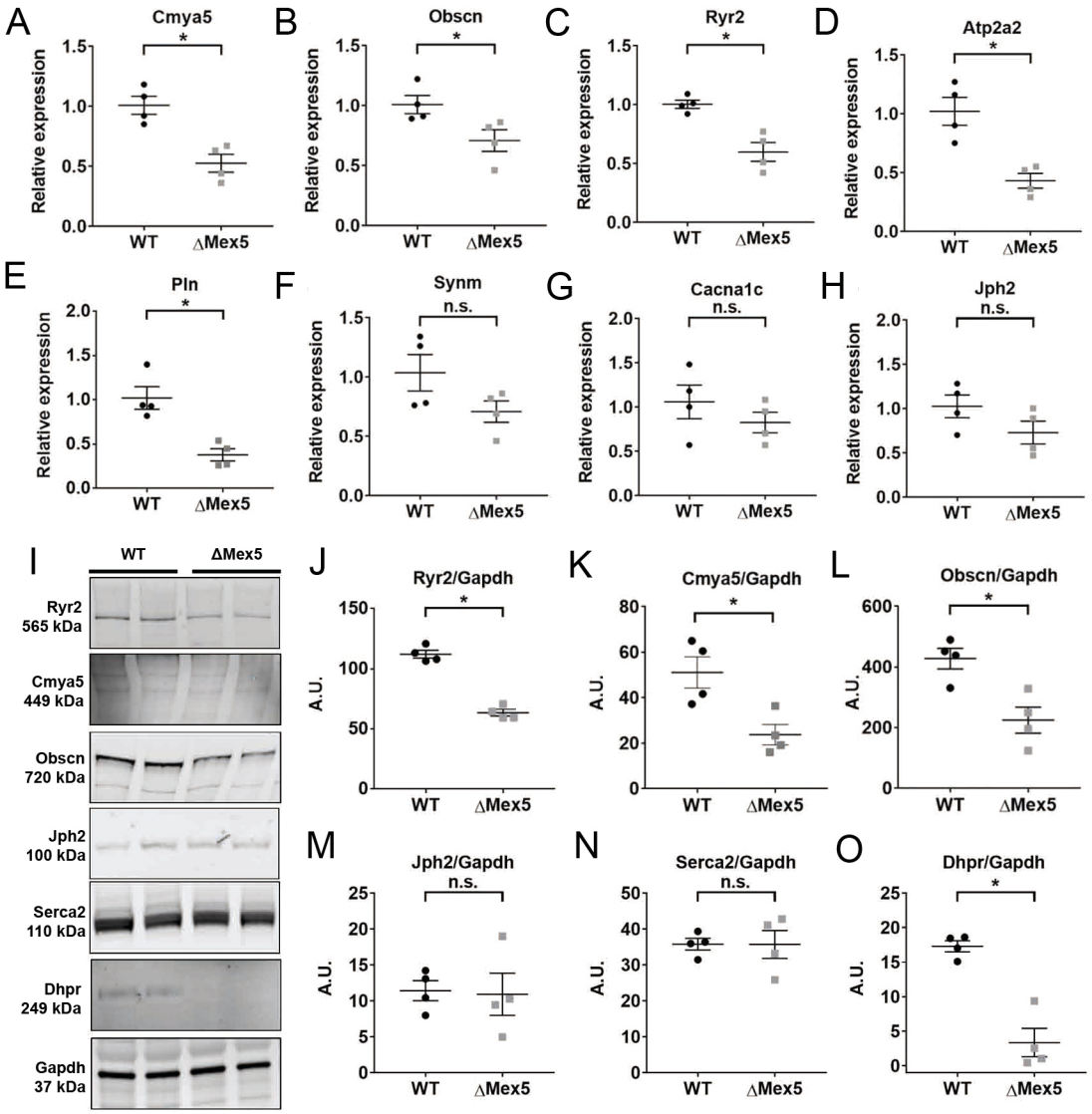

Fig. 5. Analysis of interesting dysregulated genes. (A–H) qRT-PCR results for *Cmya5*, *Obscn*, *Ryr2*, *Atp2a2*, *Pln*, *Synm*, *Cacna1c* and *Jhp2* and relative expression in WT (set at 1) and ΔMex5 mice hearts at 4 months of age. (I) Western blot analysis of Ryr2, Cmya5, Obscn, Jph2, Serca2 and Dhpr on cardiac samples from WT and ΔMex5 mice at 4 months of age. Gapdh was used for normalization (representative band showed). (J–O) Quantification of the western blot analysis for Ryr2, Cmya5, Obscn, Jph2, Serca2 and Dhpr. *$P \leq 0.05$; n.s., not significant (unpaired Mann–Whitney test was used to compare groups).

staining (Z-disc pattern) was used as sarcomeric localization control (Fig. 6A,B).

Abnormal Ryr2 and Dhpr levels are usually followed by alterations in Ca^{2+} release, one of the most common underlying mechanisms in heart failure. Often, DCM and Ca^{2+}-handling defects are associated with T-tubule remodeling, which in turns reflects on the localization of Dhprs. This delocalization creates orphaned Ryr2 on the SR, impeding its activation (Spinozzi et al., 2020; Lipsett et al., 2019). To understand whether the reduction in the expression of these two proteins could be the result of a 'feedback mechanism' due to a Ryr2 and Dhpr uncoupling, immunofluorescence analyses using antibodies against Ryr2 and Dhpr were performed. The data showed no apparent mislocalization of either Ryr2 or Dhpr in ΔMex5 hearts when compared to WT (Fig. 6C,D), suggesting absence of remodeling in either the T-tubules or the SR. Therefore, these results demonstrate a specific decrease in Ryr2 and Dhpr expression with no reorganization of either T-tubules or junctional SR.

DISCUSSION

In this study, we characterized the cardiac phenotype induced by the deletion of the is7 domain in titin. Physiological and histological analyses revealed a progressive dilation of the LV with decreased function and presence of extensive fibrosis. Morphological observations by electron microscopy showed alterations in the sarcomere, and in mitochondrial shape and organization. Finally, analyses of the molecular mechanisms responsible for the cardiac defects in ΔMex5 demonstrated that the absence of the is7 alters the sarcomeric organization of the molecule and perturbs interactions with titin partners, ultimately leading to the abnormal expression of excitation–contraction-coupling proteins.

Heart contraction and relaxation cycles are possible owing to a perfect balance of mechanical force and elasticity. At the sarcomere level, the protein that most contributes to the elasticity of the cardiomyocyte is titin. Analysis of ΔMex5 hearts indicated no change in heart stiffness, consistent with the fact that the corresponding region is not involved in mediating the elastic titin

Journal of Cell Science (2021) 134, jcs258684. doi:10.1242/jcs.258684

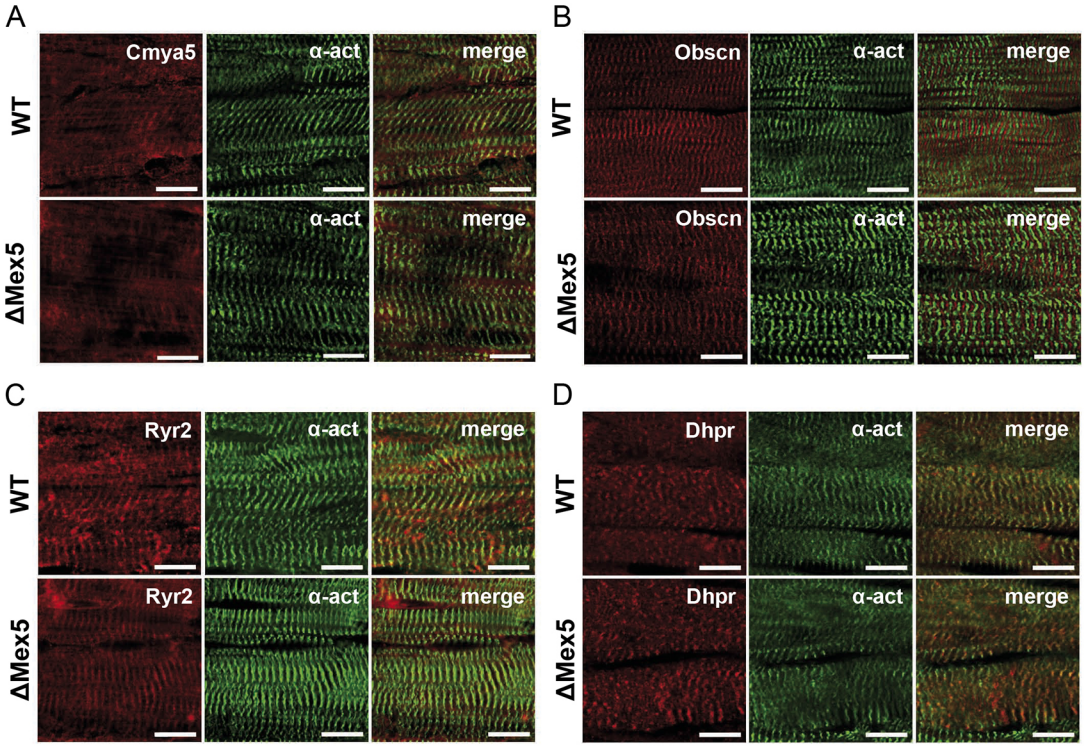

Fig. 6. Immunofluorescence staining. (A,B) Immunostaining of the M10-binding partners Cmya5 and Obscn in WT and ΔMex5 mice hearts at 4 months of age. Merge with α-actinin staining is shown. (C,D) Immunostaining of Ryr2 and Dhpr in WT and ΔMex5 mice hearts at 4 months of age. Merge with α-actinin staining is shown. Images are representative of two experiments on four samples. Scale bars: 5 µm.

properties compared to other regions of the molecule. The large sarcomere length inhomogeneity and the observed sarcomere alterations may be due to modifications of the spatial organization of the M-line segment of titin, which is known to have a role as a shock absorber (Lange et al., 2020), making the sarcomere more susceptible to contraction-induced damages. The decrease in sarcomere length could also be due to fibrosis that makes sarcomeres resistant to stretch. In addition, there is evidence of reorganization of the topology of titin domains with respect to the sarcomere. It is unlikely that the removal of is7 would be directly responsible for the observed reduction in sarcomere length because of its small size. It is more plausible that the presence or absence of the is7 determines the modality of interaction between titin and other proteins at the M-band (Lange et al., 2020). If this is the case, the altered interaction when the is7 is absent may change the anchoring of the titin molecules in the M-line, explaining the wider distance between M8M9 epitopes. Another possible explanation is that destabilization of the C-terminal part of titin, induced by the loss of the is7, bends the titin filament toward the N-terminal part, preventing it from spanning straight across the sarcomere.

Western blot analyses showed that the absence of the is7 also destabilizes the is7 adjacent domains. We previously reported that a pathological cleavage can occur in the is4–is5 regions of titin in some titinopathies (Charton et al., 2015; Sarparanta et al., 2010). Western blot analyses performed on different cells fractions did not show any pathological cleavage of titin C-terminus (data not shown), suggesting that a similar event is not happening here. Most likely, the destabilization might be due to partial degradation of the domains, rather than a ‘total’ cleavage. Intriguingly, molecular analyses showed that the is7 deletion impacts the expression of M10-binding partners of titin, Obscn and Cmya5, at both the mRNA and protein levels, as demonstrated by their downregulation in ΔMex5 hearts. Since the decrease happens for both mRNA and protein, the defect could originate solely from a transcriptional dysregulation with no change in protein stability due to the lack of protein interactions. Therefore, these data suggest a transcriptional control that adapts the level of transcript to the level of the binding domain. Interestingly, Cmya5 has previously been shown to be downregulated in tissue samples of several muscle and cardiac disorders, such as tibial muscular dystrophy, limb-girdle muscular dystrophy 2J and 2A (Sarparanta et al., 2010) and Duchenne muscular dystrophy (Tkatchenko et al., 2001). Mutations in *CMYA5* have also been associated with cardiac pathologies (Xu et al., 2015; Nakagami et al., 2007). Diverse mutations in *OBSCN* were identified to be responsible for DCM (Marston et al., 2015). Besides the sarcomere abnormalities, alterations in the expression levels of these proteins may also contribute to the phenotype, considering the role of the proteins and their implication in muscle diseases. In fact, it is well known that alterations in the interaction between Obscn and titin might results in cardiac defects (Bang et al., 2001; Grogan et al., 2020), while alterations in Obscn expression are associated with defects in SR organization and dysregulated Ca^{2+} cycling (Lange et al., 2009; Hu et al., 2017). In addition, Cmya5 interacts with Ryr2, and hence also participates in the clustering of the channel in the dyads (Benson et al., 2017). It is important to mention that Cmya5 is mainly, but not exclusively, localized in the Z-disc (Sarparanta, 2008). However, since an interaction with titin M10 domain has been demonstrated (Sarparanta et al., 2010), it cannot be excluded that variations in this interaction may reflect on the function in the Cmya5 localized in the Z-disc.

Interestingly, western blot data showed that Ryr2 and Dhpr protein levels were decreased in ΔMex5 hearts. These two proteins are strictly associated to each other in the dyad and are the main ion channels responsible for Ca^{2+} release during excitation–contraction

Journal of Cell Science (2021) 134, jcs258684. doi:10.1242/jcs.258684

coupling. The loss of is7+ titin in cardiomyocytes decreases Obscn and Cmya5 expression, and we speculate that this alteration in turn induces a downregulation of Ryr2 that sequentially alters Dhpr protein levels. Notably, it is known that a reduction in Ryr2 and Dhpr protein levels can also be the result of their uncoupling, and is induced by abnormal organization of the dyads due to T-tubules remodeling (Zhang et al., 2013). However, in our mouse model, this was not the case. In fact, additional molecular analyses of ΔMex5 cardiac tissue lysates at the protein level showed no change in the level of the junctional SR protein Jph2 or in the longitudinal SR protein Serca2, two proteins that are well known to be reduced in severe DCM where T-tubule remodeling is present (Liu et al., 2019; Spinozzi et al., 2020; Liu et al., 2020; Wu et al., 2012; Takeshima et al., 2000; Lipskaia et al., 2010). Moreover, confocal microscopy on ΔMex5 heart samples showed no localization abnormalities of either Ryr2 or Dhpr, indirectly demonstrating that dyad and T-tubule organization was not altered. Altogether, these findings allow us to assume that reduced protein expression of Ryr2 and Dhpr is most likely a direct consequence of the abnormal levels of Cmya5 and Obscn induced by the absence of the is7 in titin, rather than just a subsequent effect of the DCM phenotype.

In conclusion, preventing the cardiomyocytes from expressing their preferred titin isoforms ($Mex5^{+}$) leads to a severe cardiomyopathy, confirming that the presence of the is7 is essential for titin function in the heart. Most likely, the absence of this part of the protein destabilizes the surrounding domains and leads to the described DCM phenotype. Our data are the first to suggest a possible involvement of the titin M-line region in the regulation of excitation–contraction-coupling. Further studies on this mouse model are necessary to gain a better understanding of the potential role of titin is7 in this physiological process. Altogether, these results further stress how important the integrity of the M-line region of titin is for cardiac function and provide important insights for the identification of possible novel therapeutic targets.

MATERIAL AND METHODS

Animals

The ΔMex5 (C57BL/6N-Ttn^{gnt1}) mouse model used in this study has been previously described (Charton et al., 2016). This model was bred and housed in a barrier facility with 12-h light, 12-h dark cycles and provided food and water *ad libitum*. C57BL/6N (WT) mice, strain-matched control, were obtained from Charles River laboratories. Males were included in the study at different ages according to the experiment. All mice were handled according to the European guidelines for the human care and use of experimental animals, and animal experimentations were approved by the Ethical Committee for Animal Experimentation C2AE-51 of Evry under number APAFIS#1720 and APAFIS#19736.

For histological and molecular analysis of mouse tissues, specimens were collected immediately after animals were killed by cervical dislocation, snap frozen in liquid-nitrogen-cooled isopentane and stored at −80°C.

Echocardiography

Conventional echocardiography was performed on anesthetized mice using a Vevo 770 (Visual sonics) with a 30 MHz cardiac probe (RMV707B). During the procedure, heart rate (HR) and temperature were monitored. For echocardiography recording, sweep speed, depth, focus and gain settings were optimized to obtain the most defined acquisitions. Two-D and M-mode echocardiography were performed manually from the long parasternal axis view at the level of the largest LV diameter (at the level of the papillary level). LV dimensions [LV end-diastolic diameter (LVEDD), LV end-systolic diameter (LVESD), posterior wall (PW) and interventricular septum (IVS) wall thickness] were measured using the leading edge convention of the American Society of Echocardiography (ASE; https://www.asecho.org/guideline/ase-eae-recommendations-for-the-evaluation-of-left-ventricular-diastolic-function-by-echocardiography/). The shortening fraction (SF) and EF of the left ventricle, PW thickening (PWth) and LV mass were calculated from the above dimensions.

Pressure volume loops

In vivo pressure–volume (PV) analysis was performed in 4-month-old mice using a SciSense Advantage Admittance Derived Volume Measurement System and 1.2F catheters with 4.5 mm electrode spacing (SciSense, London, Ontario, Canada). Mice were anesthetized and ventilated with 1.5–3% isoflurane using a Physiosuite Rovent (Kent Scientific). Body temperature under anesthesia was maintained at 37°C using a Physiosuite RightTemp (Kent Scientific). A lateral incision through the skin and muscle was made below the ribcage and the diaphragm was cut in order to expose the apex of the heart. A small puncture was made in the apex of the left ventricle using a 28G needle and the 1.2F catheter was inserted into the LV. Baseline functional parameters were assessed during a pause in ventilation to avoid respiratory influences. For load-independent indices, including the end-systolic and end-diastolic PV relationships, the inferior vena cava was temporarily occluded to vary the preload conditions. Data acquisition and analysis was performed using LabScribe 3 (iWorx, Dover, NH, USA) and curve fitting was performed with MATLAB (MathWorks, Natick, MA, USA). Diastolic PV data was analyzed using a monoexponential fit with constant ($P=Ae^{\beta v}+C$) with the exponent (β) reported as the stiffness.

Electron microscopy and immunoelectron microscopy

Intact LV papillary muscles from 4-month-old male ΔMex5 mice ($n=4$) and littermate WT controls ($n=4$) were stretched from the slack length and processed for transmission electron microscopy (TEM). Briefly, fixation of cardiac tissue was performed with a mixture of 3.7% paraformaldehyde, 3% glutaraldehyde and 0.2% of tannic acid in 10 mM PBS pH 7.2 for 1 h at 4°C. This step was followed by a post-fixation in 1% OsO_4 in the same buffer for 30 min at 4°C. Samples were then dehydrated in an ethanol graded series, infiltrated with propylene oxide, and transferred to a mix of propylene oxide, Araldite 502 and Embed 812 resin, and polymerized for 48 h at 60°C. Ultrathin 90 nm longitudinal sections were obtained with a Reichert–Jung ultramicrotome and contrasted with 1% potassium permanganate and lead citrate. Specimens were observed in a TECNAI Spirit G2 transmission electron microscope (FEI, Hillsboro, OR, USA) with a side-mounted AMT Image Capture Engine V6.02 (4Mpix) digital camera operated at 100 kV. Digital images were stored for quantitative analyses of mitochondria morphology and measurements of sarcomere length with ImageJ 1.49v (NIH-USA).

Labeling of titin M-line epitopes by immunoelectron microscopy (IEM) was performed on bundles of skinned papillary muscle from WT ($n=4$) and ΔMex5 ($n=4$) mice, stretched to ∼25% in relaxing solution and processed by the pre-embedding technique previously described (Tonino et al., 2017). Cardiac tissue bundles were fixed in 3.7% paraformaldehyde in 10 mM PBS for 30 min at 4°C and, after rinsing in PBS, were incubated with glycine 50 mM in the same buffer and then blocked with 0.5% bovine serum albumin (BSA) in PBS containing protease inhibitors (0.04 mM E64 and 0.16 mM leupeptin) and 0.05% Tween 20 for 1 h at 4°C. After blocking, muscle bundles were incubated 48 h at 4°C with the following rabbit polyclonal antibodies against the following titin domains: anti-M8M9 (0.35 mg/ml; #X246; Myomedix, Germany) and anti-is7 (0.724 mg/ml; Charton et al., 2016), then followed by overnight incubation with secondary goat anti-rabbit IgG antibody conjugated to Alexa Fluor 568 (ab175471, Invitrogen, 2 mg/ml). Controls were performed in muscle bundles by replacing each primary antibody with PBS and 0.5% BSA solution containing protease inhibitors. Afterward, bundles of cardiac tissue were fixed with 3% glutaraldehyde and processed for TEM as explained above. Digital images were obtained, and M8M9 and is7 epitope distances were measured across the M-line from density plot profiles using ImageJ 1.49v (NIH, MD, USA). These values were then corrected for shrinkage (caused by the TEM procedure) using the A-band width known value of 1.6 µm (Sosa et al., 1994).

Histology and immunohistochemistry

Transverse cryosections (8 µm thickness) were prepared from frozen muscles, air dried, and stored at −80°C. Mouse sections were processed

for Hematoxylin-Phloxine-Saffron (HPS) or Sirius Red histological staining. Sections were visualized on an Axioscan Z1 automated slide scanner (Zeiss, Germany), using a Plan APO 10×0.45 NA objective. Quantification was performed by using ImageJ software.

Sections were immunostained overnight at 4°C with primary antibodies listed in Table S9. After washing three times with PBS, muscle sections were incubated with a goat secondary antibody conjugated to Alexa Fluor 594 or 647 dye (Molecular probe, dilution 1:1000) for 1 h at room temperature (RT). Sections were mounted with DAPI-fluoromount-G (SouthernBiotech) and visualized on a LEICA TCS-SP8 confocal microscope (Leica, Germany) using a 63× APO CS2 1.4 NA objective.

Light sheet imaging

Clarification of heart samples was performed by following the iDISCO clearing protocol (Renier et al., 2014). Images were acquired using an Alpha3 (α^3) Light Sheet Microscope (PhaseView, France) equipped with a XLFLUOR 2× objective, wd 340 mm, 0.14 NA (Olympus, France), and with an ORCA FLASH 4.0 SCMOS camera (Hamamatsu, Japan). Samples were immerged in a 10 ml sample chamber containing dibenzyl ether solvent (DBE). Sidewalls of the sample holder are glass coverslips (0.17 mm). Illumination arms located at each side of the sample holder create the excitation light sheet using two Plan-Neofluar 2.5× objectives (Zeiss, Germany). The sample is laid down on a motorized sample-holder, within the DBE-filled sample chamber, allowing for the three-dimensional scan of the sample. To assess heart tissue volume, heart autofluorescence was used: images were acquired using a 488 nm Laser line and to maximize the signal, no emission filters were used except for a notch filter cutting the laser wavelengths. Voxel size: 2.5×2.5×2 µm.

The QTSPIM software (PhaseView, France) was used for image acquisition. To cover the full *XY*-surface of the heart, a 2×2 tile scan was manually performed for each sample. Tile stitching was performed with IMARIS Stitcher software (Bitplane, Oxford Instruments, UK). The reconstructed stacks for each heart were processed with IMARIS software, which automatically created a three-dimensional object for volume calculations.

RNA extraction

Total RNA extraction was performed from frozen tissues by the Trizol™ method (Thermo Fisher Scientific, Waltham, MA). Extracted RNA was dissolved in 20 µl of RNase-free water and treated with Free DNA kit (Ambion) to remove residual DNA. Total RNA was quantified using a Nanodrop spectrophotometer (ND8000 Labtech, Wilmington Delaware).

RNA-sequencing

RNA from three WT 4-month-old mice and three ΔMex5 4-month-old mice hearts from mice were sequenced. RNA concentration was measured on a Nanodrop 2000 spectrophotometer (Thermo Fisher Scientific). RNA quality (RIN≥7) was controlled using an Agilent RNA 6000 Pico Kit on a 2100 Bioanalyzer instrument (Agilent Technologies). The sequencing libraries were prepared using the TruSeq Stranded Total RNA Library Prep Kit (Illumina) and sequenced according to the Illumina protocol. The reads were paired using Fastq-pair and aligned onto the mouse genome (mm10) using STAR aligner. The analysis was performed using the DESeq2 library with R software. Genes were considered as significantly dysregulated when the absolute value of log2 fold change was higher than 0.5 and adjusted *P*-value was smaller than 0.05; genes with low read count (<10) were filtered out. Gene Set Enrichement Analysis was performed using GSEABase library on R with Gene Ontology Biological Process (C5) gene sets. Ingenuity Pathway Analysis (IPA, Qiagen, Redwood City, Californiia, USA) was used to investigate enriched toxicity pathways.

qRT-PCR analyses

RNA (1 µg) was reverse-transcribed using the RevertAid H Minus First Strand cDNA Synthesis Kit (Thermo Fisher Scientific) and a mixture of random oligonucleotides and oligo-dT. Real-time PCR was performed using LightCycler480 (Roche, Basel, Switzerland) with 0.2 mM of each primer and 0.1 mM of the probe according to the protocol Absolute QPCR Rox Mix (Thermo Fisher Scientific, Waltham, MA, USA). The primers and Taqman probes (Eurogentec, Liege, Belgium) used are listed in Table S10. Data from the ubiquitous acidic ribosomal phosphoprotein (P0) was used to normalize the data across samples. The primer pairs and Taqman probes used for P0 amplification were: m181PO.F (5′-CTCCAAGCAGATGCAG-CAGA-3′), m267PO.R (5′-ACCATGATGCGCAAGGCCAT-3′) and m225PO.P (5′-CCGTGGTGCTGATGGGCAAGAA-3′). Each experiment was performed in duplicate. Quantification cycle (Cq) values were calculated with the LightCycler® 480 SW 1.5.1 using 2nd Derivative Max method.

Protein extraction, Coomassie Blue gel staining and western blotting

Proteins were extracted from LV tissues pulverized in liquid nitrogen by solubilization in urea buffer [(in mol/l): 8 urea, 2 thiourea, 0.05 Tris-HCl, 0.075 dithiothreitol with 3% SDS and 0.03% Bromophenol Blue, pH 6.8] and 50% glycerol with protease inhibitors [(in mmol/l): 0.04 E64, 0.16 leupeptin and 0.2 PMSF)] at 60°C for 10 min. Samples were centrifuged at 14,000 ***g*** for 5 min and stored at −80°C.

The titin isoform visualization was performed by loading solubilized samples on agarose gels (1%). After electrophoresis at 15 mA per gel for 3 h20, the gels were stained using Coomassie Brilliant Blue and scanned using a commercial scanner. For titin western blotting, solubilized samples were run on a 0.8% agarose gel, then transferred onto PVDF membranes using a semi-dry transfer unit (Trans-Blot Cell, Bio-Rad). Blots were stained with Ponceau S to visualize the total protein transferred. Blots were then probed with the primary antibodies listed in Table S9 followed by secondary antibodies conjugated with infrared fluorescent dyes.

For the other proteins, the samples were prepared and separated following the NuPAGE 4 to 12% Bis-Tris or 3 to 8% Tris-Acetate Gel protocol (Thermo Fisher Scientific) depending on the size of the protein, and transferred with the iBlot 2 Dry Blotting System (Thermo Fisher Scientific). Detection of proteins were performed using a standard Odyssey protocol with primary specific antibodies listed in Table S9 followed by secondary antibodies conjugated with infrared fluorescent dyes. Blots were scanned using an Odyssey Infrared Imaging System (Li-COR Biosciences). The quantification of each protein was performed in comparison to GAPDH protein quantity in the sample, using Image Studio software (Li-COR Biosciences).

Data and statistical analysis

The characterization parameters were compared between WT and ΔMex5 groups by non-parametric unpaired Mann–Whitney test. Data are expressed as mean±s.e.m. Values of $P<0.05$ were considered statistically significant. Prism package (GraphPad Software) and R software were used for data analysis.

Acknowlegments

We are grateful to Histology team of Généthon for technical support.

Competing interests

The authors declare no competing or financial interests.

Author contributions

Conceptualization: H.G., I.R; Methodology: H.G., W.L., I.R.; Software: A.B., J.C., Z.E.; Validation: A.B., S.S., H.G., W.L., I.R.; Formal analysis: A.B., S.S., P.T., J.C., J.S.; Investigation: A.B., S.S., P.T., J.S.; Data curation: A.B., Z.E.; Writing - original draft: A.B., S.S., W.L., I.R.; Writing - review & editing: A.B., S.S., P.T., J.S., Z.E., H.G., I.R.; Visualization: A.B., P.T., J.C., J.S. ; Supervision: R.K., H.G., I.R.; Project administration: A.B., S.S., W.L., I.R.; Funding acquisition: R.K., H.G., I.R.

Funding

This work was supported by the Fondation Leducq project [Mechanical Triggers to Programmed Cell Death in Cardiomyocytes – and how to prevent their Action in Failing Hearts (13CVD04)], by the European Commission MSCA-RISE-2014, H2020 Marie Skłodowska-Curie Actions staff exchange project [Muscle Stress Relief (645648)], and by National Heart, Lung, and Blood Institute grant R35HL144998. Deposited in PMC for release after 12 months.

References

Bang, M.-L., Centner, T., Fornoff, F., Geach, A. J., Gotthardt, M., Mcnabb, M., Witt, C. C., Labeit, D., Gregorio, C. C., Granzier, H. et al. (2001). The complete gene sequence of titin, expression of an unusual ≈700-kDa titin isoform, and its interaction with obscurin identify a novel Z-line to I-band linking system. *Circ. Res.* **89**, 1065-1072. doi:10.1161/hh2301.100981

Benian, G. M. and Mayans, O. (2015). Titin and obscurin: giants holding hands and discovery of a new Ig domain subset. *J. Mol. Biol.* **427**, 707-714. doi:10.1016/j.jmb.2014.12.017

Benson, M. A., Tinsley, C. L. and Blake, D. J. (2004). Myospryn is a novel binding partner for dysbindin in muscle. *J. Biol. Chem.* **279**, 10450-10458. doi:10.1074/jbc.M312664200

Benson, M. A., Tinsley, C. L., Waite, A. J., Carlisle, F. A., Sweet, S. M. M., Ehler, E., George, C. H., Lai, F. A., Martin-Rendon, E. and Blake, D. J. (2017). Ryanodine receptors are part of the myospryn complex in cardiac muscle. *Sci. Rep.* **7**, 6312. doi:10.1038/s41598-017-06395-6

Bogomolovas, J., Gasch, A., Simkovic, F., Rigden, D. J., Labeit, S. and Mayans, O. (2014). Titin kinase is an inactive pseudokinase scaffold that supports MuRF1 recruitment to the sarcomeric M-line. *Open Biol.* **4**, 140041. doi:10.1098/rsob.140041

Carmignac, V., Salih, M. A. M., Quijano-Roy, S., Marchand, S., Al Rayess, M. M., Mukhtar, M. M., Urtizberea, J. A., Labeit, S., Guicheney, P., Leturcq, F. et al. (2007). C-terminal titin deletions cause a novel early-onset myopathy with fatal cardiomyopathy. *Ann. Neurol.* **61**, 340-351. doi:10.1002/ana.21089

Charton, K., Danièle, N., Vihola, A., Roudaut, C., Gicquel, E., Monjaret, F., Tarrade, A., Sarparanta, J., Udd, B. and Richard, I. (2010). Removal of the calpain 3 protease reverses the myopathology in a mouse model for titinopathies. *Hum. Mol. Genet.* **19**, 4608-4624. doi:10.1093/hmg/ddq388

Charton, K., Sarparanta, J., Vihola, A., Milic, A., Jonson, P. H., Suel, L., Luque, H., Boumela, I., Richard, I. and Udd, B. (2015). CAPN3-mediated processing of C-terminal titin replaced by pathological cleavage in titinopathy. *Hum. Mol. Genet.* **24**, 3718-3731. doi:10.1093/hmg/ddv116

Charton, K., Suel, L., Henriques, S. F., Moussu, J. P., Bovolenta, M., Taillepierre, M., Becker, C., Lipson, K. and Richard, I. (2016). Exploiting the CRISPR/Cas9 system to study alternative splicing in vivo: application to titin. *Hum. Mol. Genet.* **25**, 4518-4532.

Chauveau, C., Rowell, J. and Ferreiro, A. (2014). A rising titan: TTN review and mutation update. *Hum. Mutat.* **35**, 1046-1059. doi:10.1002/humu.22611

Dobaczewski, M., Chen, W. and Frangogiannis, N. G. (2011). Transforming growth factor (TGF)-β signaling in cardiac remodeling. *J. Mol. Cell. Cardiol.* **51**, 600-606. doi:10.1016/j.yjmcc.2010.10.033

Fatkin, D., Mcconnell, B. K., Mudd, J. O., Semsarian, C., Moskowitz, I. G. P., Schoen, F. J., Giewat, M., Seidman, C. E. and Seidman, J. G. (2000). An abnormal Ca^{2+} response in mutant sarcomere protein–mediated familial hypertrophic cardiomyopathy. *J. Clin. Invest.* **106**, 1351-1359. doi:10.1172/JCI11093

Feng, W., Liu, C., Spinozzi, S., Wang, L., Evans, S. M. and Chen, J. (2020). Identifying the cardiac dyad proteome in vivo by a BioID2 knock-in strategy. *Circulation* **141**, 940-942. doi:10.1161/CIRCULATIONAHA.119.043434

Freiburg, A., Trombitas, K., Hell, W., Cazorla, O., Fougerousse, F., Centner, T., Kolmerer, B., Witt, C., Beckmann, J. S., Gregorio, C. C. et al. (2000). Series of exon-skipping events in the elastic spring region of titin as the structural basis for myofibrillar elastic diversity. *Circ. Res.* **86**, 1114-1121. doi:10.1161/01.RES.86.11.1114

Fukuzawa, A., Lange, S., Holt, M., Vihola, A., Carmignac, V., Ferreiro, A., Udd, B. and Gautel, M. (2008). Interactions with titin and myomesin target obscurin and obscurin-like 1 to the M-band: implications for hereditary myopathies. *J. Cell Sci.* **121**, 1841-1851. doi:10.1242/jcs.028019

Gotthardt, M., Hammer, R. E., Hubner, N., Monti, J., Witt, C. C., Mcnabb, M., Richardson, J. A., Granzier, H., Labeit, S. and Herz, J. (2003). Conditional expression of mutant M-line titins results in cardiomyopathy with altered sarcomere structure. *J. Biol. Chem.* **278**, 6059-6065. doi:10.1074/jbc.M211723200

Granzier, H. L. and Labeit, S. (2004). The giant protein titin: a major player in myocardial mechanics, signaling, and disease. *Circ. Res.* **94**, 284-295. doi:10.1161/01.RES.0000117769.88862.F8

Granzier, H. L., Radke, M. H., Peng, J., Westermann, D., Nelson, O. L., Rost, K., King, N. M. P., Yu, Q., Tschöpe, C., Mcnabb, M. et al. (2009). Truncation of titin's elastic PEVK region leads to cardiomyopathy with diastolic dysfunction. *Circ. Res.* **105**, 557-564. doi:10.1161/CIRCRESAHA.109.200964

Gregorio, C. C., Trombitás, K., Centner, T., Kolmerer, B., Stier, G., Kunke, K., Suzuki, K., Obermayr, F., Herrmann, B., Granzier, H. et al. (1998). The NH2 terminus of titin spans the Z-disc: its interaction with a novel 19-kD ligand (T-cap) is required for sarcomeric integrity. *J. Cell Biol.* **143**, 1013-1027. doi:10.1083/jcb.143.4.1013

Grogan, A., Coleman, A., Joca, H., Granzier, H., Russel, M. W., Ward, C. W. and Kontrogianni-Konstantopoulos, A. (2020). Deletion of obscurin immunoglobulin domains Ig58/59 leads to age-dependent cardiac remodeling and arrhythmia. *Basic Res. Cardiol.* **115**, 60. doi:10.1007/s00395-020-00818-8

Guo, W. and Sun, M. (2018). RBM20, a potential target for treatment of cardiomyopathy via titin isoform switching. *Biophys. Rev.* **10**, 15-25. doi:10.1007/s12551-017-0267-5

Guo, W., Bharmal, S. J., Esbona, K. and Greaser, M. L. (2010). Titin diversity—alternative splicing gone wild. *J. Biomed. Biotechnol.* **2010**, 753675. doi:10.1155/2010/753675

Gupta, M. P. (2007). Factors controlling cardiac myosin-isoform shift during hypertrophy and heart failure. *J. Mol. Cell Cardiol.* **43**, 388-403. doi:10.1016/j.yjmcc.2007.07.045

Hackman, P., Marchand, S., Sarparanta, J., Vihola, A., Penisson-Besnier, I., Eymard, B., Pardal-Fernández, J. M., Hammouda, E.-H., Richard, I., Illa, I. et al. (2008). Truncating mutations in C-terminal titin may cause more severe tibial muscular dystrophy (TMD). *Neuromuscul. Disord.* **18**, 922-928. doi:10.1016/j.nmd.2008.07.010

Hanna, A. and Frangogiannis, N. G. (2019). The Role of the TGF-β Superfamily in Myocardial Infarction. *Front. Cardiovasc. Med.* **6**, 140. doi:10.3389/fcvm.2019.00140

Heymans, S., Schroen, B., Vermeersch, P., Milting, H., Gao, F., Kassner, A., Gillijns, H., Herijgers, P., Flameng, W., Carmeliet, P. et al. (2005). Increased cardiac expression of tissue inhibitor of metalloproteinase-1 and tissue inhibitor of metalloproteinase-2 is related to cardiac fibrosis and dysfunction in the chronic pressure-overloaded human heart. *Circulation* **112**, 1136-1144. doi:10.1161/CIRCULATIONAHA.104.516963

Houweling, A. C., Van Borren, M. M., Moorman, A. F. M. and Christoffels, V. M. (2005). Expression and regulation of the atrial natriuretic factor encoding gene Nppa during development and disease. *Cardiovasc. Res.* **67**, 583-593. doi:10.1016/j.cardiores.2005.06.013

Hu, L.-Y. R., Ackermann, M. A. and Kontrogianni-Konstantopoulos, A. (2015). The sarcomeric M-region: a molecular command center for diverse cellular processes. *Biomed. Res. Int.* **2015**, 714197. doi:10.1155/2015/714197

Hu, L.-Y. R., Ackermann, M. A., Hecker, P. A., Prosser, B. L., King, B., O'connell, K. A., Grogan, A., Meyer, L. C., Berndsen, C. E., Wright, N. T. et al. (2017). Deregulated Ca^{2+} cycling underlies the development of arrhythmia and heart disease due to mutant obscurin. *Sci. Adv.* **3**, e1603081. doi:10.1126/sciadv.1603081

Jäckel, M., Witt, C., Antonova, O., Curdt, I., Labeit, S. and Jockusch, H. (1997). Deletion in the Z-line region of the titin gene in a baby hamster kidney cell line, BHK-21-Bi. *FEBS Lett.* **408**, 21-24. doi:10.1016/S0014-5793(97)00381-5

Kolmerer, B., Olivieri, N., Witt, C. C., Herrmann, B. G. and Labeit, S. (1996). Genomic organization of M line titin and its tissue-specific expression in two distinct isoforms. *J. Mol. Biol.* **256**, 556-563. doi:10.1006/jmbi.1996.0108

Koss, K. L., Grupp, I. L. and Kranias, E. G. (1997). The relative phospholamban and SERCA2 ratio: a critical determinant of myocardial contractility. *Basic Res. Cardiol.* **92** Suppl. 1, 17-24. doi:10.1007/BF00794064

Labeit, S. and Kolmerer, B. (1995). Titins: giant proteins in charge of muscle ultrastructure and elasticity. *Science* **270**, 293-296. doi:10.1126/science.270.5234.293

Labeit, S., Lahmers, S., Burkart, C., Fong, C., Mcnabb, M., Witt, S., Witt, C., Labeit, D. and Granzier, H. (2006). Expression of distinct classes of titin isoforms in striated and smooth muscles by alternative splicing, and their conserved interaction with filamins. *J. Mol. Biol.* **362**, 664-681. doi:10.1016/j.jmb.2006.07.077

Lange, S., Auerbach, D., Mcloughlin, P., Perriard, E., Schäfer, B. W., Perriard, J.-C. and Ehler, E. (2002). Subcellular targeting of metabolic enzymes to titin in heart muscle may be mediated by DRAL/FHL-2. *J. Cell Sci.* **115**, 4925-4936. doi:10.1242/jcs.00181

Lange, S., Ouyang, K., Meyer, G., Cui, L., Cheng, H., Lieber, R. L. and Chen, J. (2009). Obscurin determines the architecture of the longitudinal sarcoplasmic reticulum. *J. Cell Sci.* **122**, 2640-2650. doi:10.1242/jcs.046193

Lange, S., Pinotsis, N., Agarkova, I. and Ehler, E. (2020). The M-band: the underestimated part of the sarcomere. *Biochim. Biophys. Acta Mol. Cell Res.* **1867**, 118440.

Linke, W. A., Rudy, D. E., Centner, T., Gautel, M., Witt, C., Labeit, S. and Gregorio, C. C. (1999). I-band titin in cardiac muscle is a three-element molecular spring and is critical for maintaining thin filament structure. *J. Cell Biol.* **146**, 631-644. doi:10.1083/jcb.146.3.631

Lipsett, D. B., Frisk, M., Aronsen, J. M., Nordén, E. S., Buonarati, O. R., Cataliotti, A., Hell, J. W., Sjaastad, I., Christensen, G. and Louch, W. E. (2019). Cardiomyocyte substructure reverts to an immature phenotype during heart failure. *J. Physiol.* **597**, 1833-1853. doi:10.1113/JP277273

Lipskaia, L., Chemaly, E. R., Hadri, L., Lompre, A.-M. and Hajjar, R. J. (2010). Sarcoplasmic reticulum Ca^{2+} ATPase as a therapeutic target for heart failure. *Expert Opin. Biol. Ther.* **10**, 29-41. doi:10.1517/14712590903321462

Liu, C., Spinozzi, S., Chen, J.-Y., Fang, X., Feng, W., Perkins, G., Cattaneo, P., Guimarães-Camboa, N., Dalton, N. D., Peterson, K. L. et al. (2019). Nexilin is a new component of junctional membrane complexes required for cardiac T-tubule formation. *Circulation* **140**, 55-66. doi:10.1161/CIRCULATIONAHA.119.039751

Liu, C., Spinozzi, S., Feng, W., Chen, Z., Zhang, L., Zhu, S., Wu, T., Fang, X., Ouyang, K., Evans, S. M. et al. (2020). Homozygous G650del nexilin variant

causes cardiomyopathy in mice. *JCI Insight* **5**, 138780. doi:10.1172/jci.insight.138780

Lostal, W., Roudaut, C., Faivre, M., Charton, K., Suel, L., Bourg, N., Best, H., Smith, J. E., Gohlke, J., Corre, G. et al. (2019). Titin splicing regulates cardiotoxicity associated with calpain 3 gene therapy for limb-girdle muscular dystrophy type 2A. *Sci. Transl. Med.* **11**, eaat6072. doi:10.1126/scitranslmed.aat6072

Marston, S., Montgiraud, C., Munster, A. B., Copeland, O., Choi, O., Dos Remedios, C., Messer, A. E., Ehler, E. and Knöll, R. (2015). OBSCN mutations associated with dilated cardiomyopathy and haploinsufficiency. *PLoS ONE* **10**, e0138568. doi:10.1371/journal.pone.0138568

Mártonfalvi, Z., Bianco, P., Linari, M., Caremani, M., Nagy, A., Lombardi, V. and Kellermayer, M. (2014). Low-force transitions in single titin molecules reflect a memory of contractile history. *J. Cell Sci.* **127**, 858-870. doi:10.1242/jcs.138461

Meurs, K. M., Friedenberg, S. G., Kolb, J., Saripalli, C., Tonino, P., Woodruff, K., Olby, N. J., Keene, B. W., Adin, D. B., Yost, O. L. et al. (2019). A missense variant in the titin gene in Doberman pinscher dogs with familial dilated cardiomyopathy and sudden cardiac death. *Hum. Genet.* **138**, 515-524. doi:10.1007/s00439-019-01973-2

Montgomery, R. L., Hullinger, T. G., Semus, H. M., Dickinson, B. A., Seto, A. G., Lynch, J. M., Stack, C., Latimer, P. A., Olson, E. N. and Van Rooij, E. (2011). Therapeutic inhibition of miR-208a improves cardiac function and survival during heart failure. *Circulation* **124**, 1537-1547. doi:10.1161/CIRCULATIONAHA.111.030932

Musa, H., Meek, S., Gautel, M., Peddie, D., Smith, A. J. H. and Peckham, M. (2006). Targeted homozygous deletion of M-band titin in cardiomyocytes prevents sarcomere formation. *J. Cell Sci.* **119**, 4322-4331. doi:10.1242/jcs.03198

Nakagami, H., Kikuchi, Y., Katsuya, T., Morishita, R., Akasaka, H., Saitoh, S., Rakugi, H., Kaneda, Y., Shimamoto, K. and Ogihara, T. (2007). Gene polymorphism of myospryn (cardiomyopathy-associated 5) is associated with left ventricular wall thickness in patients with hypertension. *Hypertens. Res.* **30**, 1239-1246. doi:10.1291/hypres.30.1239

Nusayr, E., Strom, J., Slater, R. E. and Granzier, H. L. (2018). A novel mouse model for titin-based dilated cardiomyopathy. *Biophys. J.* **114**, 312a-313a. doi:10.1016/j.bpj.2017.11.1765

Pask, H. T., Jones, K. L., Luther, P. K. and Squire, J. M. (1994). M-band structure, M-bridge interactions and contraction speed in vertebrate cardiac muscles. *J. Muscle Res. Cell Motil.* **15**, 633-645. doi:10.1007/BF00121071

Prudner, B. C., Roy, P. S., Damron, D. S. and Russell, M. A. (2014). α-Synemin localizes to the M-band of the sarcomere through interaction with the M10 region of titin. *FEBS Lett.* **588**, 4625-4630. doi:10.1016/j.febslet.2014.11.001

Puchner, E. M., Alexandrovich, A., Kho, A. L., Hensen, U., Schafer, L. V., Brandmeier, B., Grater, F., Grubmuller, H., Gaub, H. E. and Gautel, M. (2008). Mechanoenzymatics of titin kinase. *Proc. Natl. Acad. Sci. USA* **105**, 13385-13390. doi:10.1073/pnas.0805034105

Radke, M. H., Peng, J., Wu, Y., Mcnabb, M., Nelson, O. L., Granzier, H. and Gotthardt, M. (2007). Targeted deletion of titin N2B region leads to diastolic dysfunction and cardiac atrophy. *Proc. Natl. Acad. Sci. USA* **104**, 3444-3449. doi:10.1073/pnas.0608543104

Radke, M. H., Polack, C., Methawasin, M., Fink, C., Granzier, H. L. and Gotthardt, M. (2019). Deleting full length titin versus the titin M-band region leads to differential mechanosignaling and cardiac phenotypes. *Circulation* **139**, 1813-1827. doi:10.1161/CIRCULATIONAHA.118.037588

Renier, N., Wu, Z., Simon, D. J., Yang, J., Ariel, P. and Tessier-Lavigne, M. (2014). iDISCO: a simple, rapid method to immunolabel large tissue samples for volume imaging. *Cell* **159**, 896-910. doi:10.1016/j.cell.2014.10.010

Richard, I., Broux, O., Allamand, V., Fougerousse, F., Chiannilkulchai, N., Bourg, N., Brenguier, L., Devaud, C., Pasturaud, P., Roudaut, C. et al. (1995). Mutations in the proteolytic enzyme calpain 3 cause limb-girdle muscular dystrophy type 2A. *Cell* **81**, 27-40. doi:10.1016/0092-8674(95)90368-2

Roberts, A. M., Ware, J. S., Herman, D. S., Schafer, S., Baksi, J., Bick, A. G., Buchan, R. J., Walsh, R., John, S., Wilkinson, S. et al. (2015). Integrated allelic, transcriptional, and phenomic dissection of the cardiac effects of titin truncations in health and disease. *Sci. Transl. Med.* **7**, 270ra6. doi:10.1126/scitranslmed.3010134

Sarparanta, J. (2008). Biology of myospryn: what's known? *J. Muscle Res. Cell Motil.* **29**, 177-180. doi:10.1007/s10974-008-9165-6

Sarparanta, J., Blandin, G., Charton, K., Vihola, A., Marchand, S., Milic, A., Hackman, P., Ehler, E., Richard, I. and Udd, B. (2010). Interactions with M-band titin and calpain 3 link myospryn (CMYA5) to tibial and limb-girdle muscular dystrophies. *J. Biol. Chem.* **285**, 30304-30315. doi:10.1074/jbc.M110.108720

Schafer, S., De Marvao, A., Adami, E., Fiedler, L. R., Ng, B., Khin, E., Rackham, O. J. L., Van Heesch, S., Pua, C. J., Kui, M. et al. (2017). Titin-truncating variants affect heart function in disease cohorts and the general population. *Nat. Genet.* **49**, 46-53. doi:10.1038/ng.3719

Sosa, H., Popp, D., Ouyang, G. and Huxley, H. E. (1994). Ultrastructure of skeletal muscle fibers studied by a plunge quick freezing method: myofilament lengths. *Biophys. J.* **67**, 283-292. doi:10.1016/S0006-3495(94)80479-5

Spinozzi, S., Liu, C., Chen, Z., Feng, W., Zhang, L., Ouyang, K., Evans, S. M. and Chen, J. (2020). Nexilin is necessary for maintaining the transverse-axial tubular system in adult cardiomyocytes. *Circ. Heart Fail.* **13**, e006935. doi:10.1161/CIRCHEARTFAILURE.120.006935

Stöhr, E. J., Takayama, H. and Ferrari, G. (2018). Stretch your heart—but not too far: the role of titin mutations in dilated cardiomyopathy. *J. Thorac. Cardiovasc. Surg.* **156**, 209-214. doi:10.1016/j.jtcvs.2017.10.160

Takawale, A., Zhang, P., Patel, V. B., Wang, X., Oudit, G. and Kassiri, Z. (2017). Tissue Inhibitor of Matrix Metalloproteinase-1 Promotes Myocardial Fibrosis by Mediating CD63-Integrin β1 Interaction. *Hypertension* **69**, 1092-1103. doi:10.1161/HYPERTENSIONAHA.117.09045

Takeshima, H., Komazaki, S., Nishi, M., Iino, M. and Kangawa, K. (2000). Junctophilins: a novel family of junctional membrane complex proteins. *Mol. Cell* **6**, 11-22.

Tayal, U., Newsome, S., Buchan, R., Whiffin, N., Walsh, R., Barton, P. J., Ware, J. S., Cook, S. A. and Prasad, S. K. (2017). Truncating variants in titin independently predict early arrhythmias in patients with dilated cardiomyopathy. *J. Am. Coll. Cardiol.* **69**, 2466-2468. doi:10.1016/j.jacc.2017.03.530

Tkatchenko, A. V., Piétu, G., Cros, N., Gannoun-Zaki, L., Auffray, C., Léger, J. J. and Dechesne, C. A. (2001). Identification of altered gene expression in skeletal muscles from Duchenne muscular dystrophy patients. *Neuromuscul. Disord.* **11**, 269-277. doi:10.1016/S0960-8966(00)00198-X

Tonino, P., Kiss, B., Strom, J., Methawasin, M., Smith, J. E., III, Kolb, J., Labeit, S. and Granzier, H. (2017). The giant protein titin regulates the length of the striated muscle thick filament. *Nat. Commun.* **8**, 1041. doi:10.1038/s41467-017-01144-9

Van Der Ven, P. F. M. and Fürst, D. O. (1997). Assembly of titin, myomesin and M-protein into the sarcomeric M band in differentiating human skeletal muscle cells in vitro. *Cell Struct. Funct.* **22**, 163-171. doi:10.1247/csf.22.163

Vanderheyden, M., Mullens, W., Delrue, L., Goethals, M., De Bruyne, B., Wijns, W., Geelen, P., Verstreken, S., Wellens, F. and Bartunek, J. (2008). Myocardial gene expression in heart failure patients treated with cardiac resynchronization therapy: responders versus nonresponders. *J. Am. Coll Cardiol.* **51**, 129-136. doi:10.1016/j.jacc.2007.07.087

Weinert, S., Bergmann, N., Luo, X., Erdmann, B. and Gotthardt, M. (2006). M line-deficient titin causes cardiac lethality through impaired maturation of the sarcomere. *J. Cell Biol.* **173**, 559-570. doi:10.1083/jcb.200601014

Wu, H.-D., Xu, M., Li, R.-C., Guo, L., Lai, Y.-S., Xu, S.-M., Li, S.-F., Lü, Q.-L., Li, L.-L., Zhang, H.-B. et al. (2012). Ultrastructural remodelling of Ca^{2+} signalling apparatus in failing heart cells. *Cardiovasc. Res.* **95**, 430-438. doi:10.1093/cvr/cvs195

Xu, J., Li, Z., Ren, X., Dong, M., Li, J., Shi, X., Zhang, Y., Xie, W., Sun, Z., Liu, X. et al. (2015). Investigation of pathogenic genes in chinese sporadic hypertrophic cardiomyopathy patients by whole exome sequencing. *Sci. Rep.* **5**, 16609. doi:10.1038/srep16609

Zhang, H.-B., Li, R.-C., Xu, M., Xu, S.-M., Lai, Y.-S., Wu, H.-D., Xie, X.-J., Gao, W., Ye, H., Zhang, Y.-Y. et al. (2013). Ultrastructural uncoupling between T-tubules and sarcoplasmic reticulum in human heart failure. *Cardiovasc. Res.* **98**, 269-276. doi:10.1093/cvr/cvt030

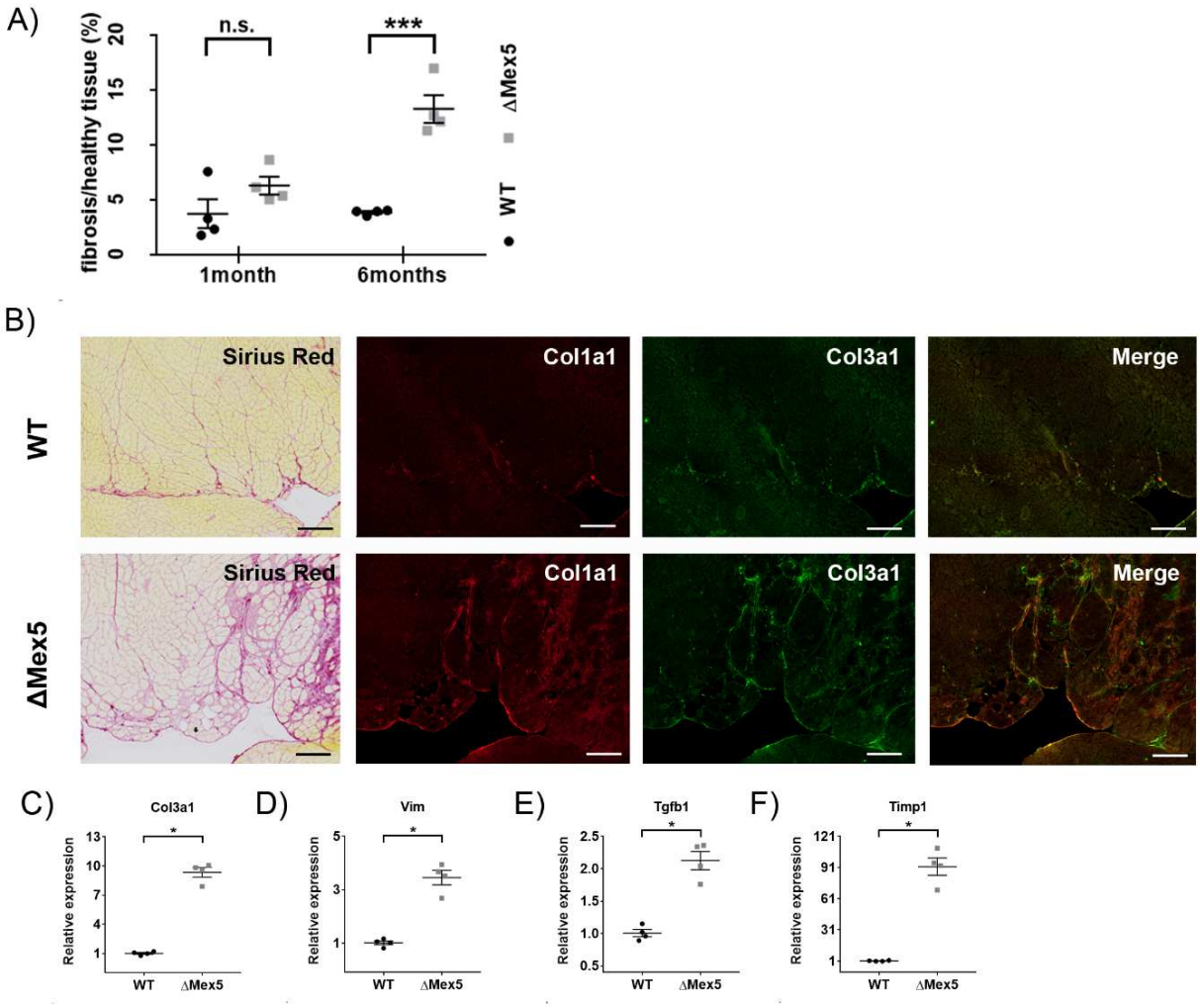

Fig. S1. A) Sirius red staining quantification at 1 and 6 months. Amount of staining is quantified in percentage of the total tissue section (mean ± SEM). **B)** Histological sections of heart from Wild Type and ΔMex5 mice by Sirius Red at 4 months. Immunostaining of Collagen1a1 and Collagen 3a1 in Wild Type and ΔMex5 mice hearts at 4 months. Merge. Scale bars, 100 µm. **C)**, **D)**, **E)**, **F)** qPCR results for fibrosis and heart damage makers (Co3a1, Vim, Tgfβ1, Timp1) relative expression in Wild Type and ΔMex5 mice hearts at 4 months.

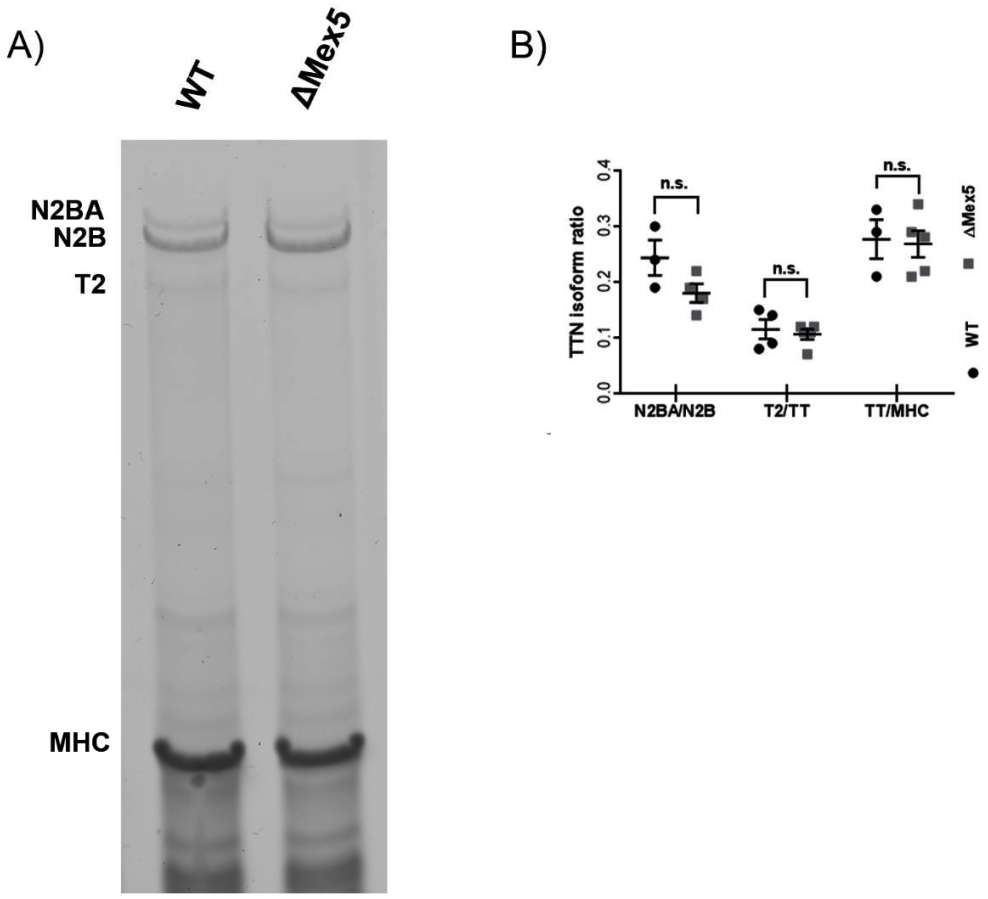

Fig. S2. A) Coomassie Blue gel staining on cardiac samples from Wild Type and ΔMex5 mice at 4 months. T2 = titin degradation products. **B**) Quantification of Coomassie Blue gel. Results are presented in means ± SEM. Unpaired Mann-Whitney test were used to compare groups.

Table S1. Echocardiographic parameters for WT and ΔMex5 mice at different ages. Results are presented in means ± SEM. Unpaired Mann-Whitney test were used to compare groups, * P ≤ 0.05, ** P ≤ 0.01.

		2 months	4 months	13 months
Mice number	WT	n = 7	n = 11	n = 6
	ΔMex5	n = 6	n = 8	n = 7
Heart rate (bpm)	WT	454 ± 19	472 ± 24	484 ± 23
	ΔMex5	469 ± 17	466 ± 23	462 ± 34
LV/body mass ratio	WT	4.8 ± 0.1	4.9 ± 0.2	4.3 ± 0.3
	ΔMex5	5.1 ± 0.2	5.4 ± 0.3	5.0 ± 0.4
Left Ventricule Internal Diameter end Diastole (mm)	WT	4.47 ± 0.09	4.28 ± 0.09	4.42 ± 0.13
	ΔMex5	4.74 ± 0,11	**4.83 ± 0.22** **	**5.23 ± 0.17** **
Left Ventricule Internal Diameter end Systole (mm)	WT	3.59 ± 0.12	3.13 ± 0.12	3.28 ± 0.16
	ΔMex5	4.04 ± 0.18	**3.88 ± 0.26** **	**4.24 ± 0.21** **
LV posterior wall (mm)	WT	0.59 ± 0.02	0.77 ± 0.03	0.88 ± 0.06
	ΔMex5	0.57 ± 0.03	0.83 ± 0.07	0.75 ± 0.06
Intra ventricular septum (mm)	WT	0.80 ± 0.01	0.90 ± 0.04	0.96 ± 0.03
	ΔMex5	0.78 ± 0.03	1.00 ± 0.05	0.88 ± 0.05
Shortening Fraction (%)	WT	20 ± 1	27 ± 2	26 ± 1
	ΔMex5	15 ± 2	**20 ± 3** *	**19 ± 2** *

Table S2. Measures of pressure/volumes parameters for WT and ΔMex5 mice at 4 months. Results are presented in means ± SEM. EDPVR **:** End Diastolic Pressure Volume Relationship. Unpaired Mann-Whitney test were used to compare groups.

Mice number	WT	n	=	5		
	ΔMex5	n	=	5		
Heart rate (bpm)	WT	515	±	24		
	ΔMex5	470	±	25	$p = 0.421$	
End Systolic Elastance (mmHg/µL)	WT	4.08	±	0.66		
	ΔMex5	2.51	±	0.67	$p = 0.151$	
EDPVR – β (mmHg/µL)	WT	0.03	±	0.01		
	ΔMex5	0.03	±	0.00	$p = 0.548$	
End Systolic Volume (µL)	WT	26	±	4		
	ΔMex5	**56**	**±**	**11**	$\mathbf{p = 0.032}$	*
End Diastolic Volume (µL)	WT	67	±	5		
	ΔMex5	91	±	11	$p = 0.095$	
Stroke Volume (µL)	WT	40	±	3		
	ΔMex5	35	±	1	$p = 0.151$	
End Systolic Pressure (mmHg)	WT	90	±	4		
	ΔMex5	89	±	4	$p = 0.841$	
End Diastolic Pressure (mmHg)	WT	2	±	0		
	ΔMex5	**5**	**±**	**1**	$\mathbf{p = 0.032}$	*
dP/dtmin (mmHg/sec)	WT	- 7733	±	726		
	ΔMex5	- 6823	±	554	$p = 0.310$	
dP/dtmax (mmHg/sec)	WT	9155	±	984		
	ΔMex5	7903	±	562	$p = 0.310$	
Ejection Fraction (SV/EDV)	WT	61	±	3		
	ΔMex5	**41**	**±**	**5**	$\mathbf{p = 0.016}$	*

Table S3. Top 25 up regulated genes identified in RNAseq analysis of ΔMex5 mice versus WT at 4 months. Results are sorted by absolute value of log2FC.

Gene name	log2FC	pValue	Mean WT	Mean ΔMex5
Spp1	6.60	5.3E-128	6.65	2162.74
Cilp	4.77	4.7E-278	109.77	3357.31
Ltbp2	4.74	3.0E-174	68.03	2206.18
Gpnmb	4.68	1.6E-97	19.98	764.57
Sprr1a	4.33	1.4E-36	1.39	222.75
Tnc	4.28	3.0E-33	38.66	4363.96
Timp1	3.98	5.7E-52	24.25	625.54
Col12a1	3.82	2.1E-60	50.08	989.43
Col8a2	3.74	3.3E-40	10.59	247.08
Sfrp2	3.62	2.1E-55	30.20	501.17
Thbs4	3.61	3.8E-121	66.85	919.77
Ptn	3.40	1.3E-35	17.60	290.91
Postn	3.35	1.7E-21	414.51	12040.11
Mfap4	3.31	4.0E-57	35.05	428.05
Piezo2	3.27	2.9E-31	13.45	209.01
Col3a1	3.22	1.7E-61	3682.59	40685.43
Col14a1	3.20	9.5E-116	207.54	2081.22
Ctss	3.19	3.0E-59	162.81	1773.00
Trem2	3.16	2.9E-28	17.93	259.21
Atp6v0d2	3.15	2.7E-17	0.67	58.07
Apol7d	3.15	5.2E-32	41.67	541.35
Lgals3	3.10	7.0E-19	35.14	747.38
Mpeg1	3.09	8.8E-23	143.04	2205.83
Dkk3	3.01	2.8E-32	27.12	299.63
P4ha3	2.96	1.6E-14	0.33	54.09

Table S4. Top 25 down regulated genes identified in RNAseq analysis of ΔMex5 mice versus WT at 4 months. Results are sorted by absolute value of log2FC.

Gene name	log2FC	pValue	Mean WT	Mean ΔMex5
Osbpl6	-1.76	2.3E-21	515.48	140.16
Zfp619	-1.58	1.9E-08	103.02	28.98
Pde11a	-1.56	2.7E-04	21.94	1.85
Lgals4	-1.49	0.001	561.89	85.54
Mylk4	-1.42	1.6E-21	2880.01	1036.29
Rtn4r	-1.40	7.2E-06	75.68	23.33
Ano5	-1.39	1.4E-05	80.70	24.81
Sv2c	-1.39	2.5E-04	38.48	10.09
Pah	-1.35	0.002	19.93	3.24
Kcnv2	-1.32	1.3E-07	279.05	100.09
mt-Ts1	-1.29	0.002	333.81	84.07
Pop4	-1.26	1.6E-07	138.11	52.85
Wnk2	-1.24	3.6E-21	1894.07	782.52
Clcn1	-1.18	5.5E-10	256.20	106.65
Whrn	-1.16	8.3E-10	398.94	168.86
Pzp	-1.16	0.006	32.33	9.46
Celsr3	-1.16	5.7E-06	107.32	43.91
Clec18a	-1.13	0.008	34.03	10.35
Lrrc52	-1.11	0.001	73.90	28.82
mt-Ti	-1.09	5.0E-23	4813.41	2232.44
Ctla4	-1.08	0.002	59.32	23.36
Apob	-1.08	0.015	22.66	1.83
Lmntd1	-1.06	0.015	26.52	8.54
Gal3st3	-1.05	8.7E-06	236.70	106.10
mt-Tm	-1.04	5.9E-07	2037.16	939.00

Table S5. Top 25 up regulated GO biological processes identified in RNAseq analysis of ΔMex5 mice versus WT at 4 months.

Gene Set ID	set Size	NES	pValue adjusted
GO_EXTRACELLULAR_STRUCTURE_ORGANIZATION	319	2.087	2.40E-34
GO_LEUKOCYTE_MIGRATION	330	2.014	1.24E-28
GO_REGULATION_OF_CELL_ACTIVATION	437	1.890	1.69E-25
GO_MYELOID_LEUKOCYTE_MEDIATED_IMMUNITY	451	1.835	2.95E-22
GO_LEUKOCYTE_DIFFERENTIATION	401	1.856	3.71E-22
GO_ADAPTIVE_IMMUNE_RESPONSE	273	1.966	3.07E-20
GO_POSITIVE_REGULATION_OF_IMMUNE_RESPONSE	480	1.773	2.07E-19
GO_WOUND_HEALING	412	1.800	2.07E-19
GO_POSITIVE_REGULATION_OF_CYTOKINE_PRODUCTION	356	1.844	5.70E-19
GO_T_CELL_ACTIVATION	354	1.834	8.88E-19
GO_POSITIVE_REGULATION_OF_CELL_ACTIVATION	264	1.938	2.31E-18
GO_POSITIVE_REGULATION_OF_CELLULAR_COMPONENT_MOVEMENT	476	1.740	5.31E-18
GO_CELL_CHEMOTAXIS	226	1.956	2.30E-17
GO_MYELOID_LEUKOCYTE_MIGRATION	158	2.090	2.30E-17
GO_PHAGOCYTOSIS	227	1.960	4.18E-17
GO_REGULATION_OF_INFLAMMATORY_RESPONSE	275	1.894	4.25E-17
GO_POSITIVE_REGULATION_OF_RESPONSE_TO_EXTERNAL_STIMULUS	397	1.767	4.95E-17
GO_POSITIVE_REGULATION_OF_CELL_ADHESION	330	1.823	9.15E-17
GO_REGULATION_OF_LYMPHOCYTE_ACTIVATION	333	1.821	1.86E-16
GO_SISTER_CHROMATID_SEGREGATION	169	2.028	3.91E-16
GO_LEUKOCYTE_CHEMOTAXIS	168	2.019	1.08E-15
GO_TAXIS	485	1.701	1.47E-15
GO_REGULATION_OF_LEUKOCYTE_MIGRATION	167	2.015	1.50E-15
GO_MITOTIC_SISTER_CHROMATID_SEGREGATION	146	2.063	1.81E-15
GO_RESPONSE_TO_BACTERIUM	410	1.726	2.76E-15

Table S6. Top 25 down regulated GO biological processes identified in RNAseq analysis of ΔMex5 mice versus WT at 4 months.

Gene Set ID	set Size	NES	pValue adjusted
GO_MITOCHONDRIAL_RESPIRATORY_CHAIN_ COMPLEX_ASSEMBLY	99	-3.478	1.77E-22
GO_RESPIRATORY_ELECTRON_TRANSPORT_CHAIN	110	-3.234	1.15E-20
GO_AEROBIC_RESPIRATION	82	-3.338	5.52E-19
GO_MITOCHONDRIAL_ELECTRON_TRANSPORT_NADH_ TO_UBIQUINONE	52	-3.340	6.52E-19
GO_ATP_SYNTHESIS_COUPLED_ELECTRON_TRANSPOR T	92	-3.376	2.84E-18
GO_NADH_DEHYDROGENASE_COMPLEX_ASSEMBLY	63	-3.317	8.40E-18
GO_MITOCHONDRIAL_TRANSLATIONAL_TERMINATION	89	-3.233	8.09E-17
GO_TRANSLATIONAL_TERMINATION	102	-3.126	3.07E-15
GO_TRICARBOXYLIC_ACID_CYCLE	32	-3.001	5.23E-11
GO_INNER_MITOCHONDRIAL_MEMBRANE_ ORGANIZATION	51	-2.865	1.50E-10
GO_MITOCHONDRIAL_TRANSMEMBRANE_TRANSPORT	96	-2.680	5.44E-10
GO_FATTY_ACID_BETA_OXIDATION	64	-2.747	3.49E-09
GO_MONOCARBOXYLIC_ACID_CATABOLIC_PROCESS	108	-2.469	2.76E-08
GO_CRISTAE_FORMATION	34	-2.803	4.41E-08
GO_ATP_SYNTHESIS_COUPLED_PROTON_TRANSPORT	25	-2.678	1.55E-07
GO_FATTY_ACID_CATABOLIC_PROCESS	93	-2.421	2.94E-07
GO_2_OXOGLUTARATE_METABOLIC_PROCESS	14	-2.475	1.06E-06
GO_CELLULAR_AMINO_ACID_CATABOLIC_PROCESS	91	-2.279	4.26E-06
GO_FATTY_ACID_BETA_OXIDATION_USING_ACYL_ COA_DEHYDROGENASE	11	-2.383	5.31E-06
GO_PROTEIN_TRANSMEMBRANE_IMPORT_INTO_ INTRACELLULAR_ORGANELLE	33	-2.521	1.49E-05
GO_LIPID_OXIDATION	92	-2.199	1.89E-05
GO_THIOESTER_METABOLIC_PROCESS	82	-2.209	2.03E-05
GO_MITOCHONDRIAL_RNA_METABOLIC_PROCESS	43	-2.407	2.39E-05
GO_MITOCHONDRIAL_ELECTRON_TRANSPORT_ UBIQUINOL_TO_CYTOCHROME_C	13	-2.336	2.81E-05
GO_AEROBIC_ELECTRON_TRANSPORT_CHAIN	20	-2.410	2.85E-05

Table S7. M10 Binding partner values obtained by RNAseq analysis of ΔMex5 mice versus WT at 4 months.

Gene name	Protein	log2FC	pValue	Mean WT	Mean ΔMex5
Capn3	Calpain3	0.19	0.636	92.67	107.19
Cmya5	Cardiomyopathy associated protein 5	-0.58	**4.0E-04**	37053.21	24367.82
Obscn	Obscurin	-0.44	**0.001**	44418.89	32389.48
Obsl1	Obscurin like-1	-0.27	**0.028**	2143.24	1770.10
Synm	alpha-synemin	0.32	0.112	285.49	360.00

Table S8. Genes with a role in Ca2+-signaling. Values obtained by RNAseq analysis of ΔMex5 mice versus WT at 4 months.

Gene name	Protein	log2FC	pValue	Mean WT	Mean ΔMex5
Atp2a2	Serca2	-0.58	**1.6E-06**	266940.42	177612.55
Cacna1c	Dihydropyridine receptor	-0.25	0.057	10077.29	8462.90
Jph2	Junctophilin 2	-0.42	**0.001**	7420.52	5525.69
Pln	Phospholamban	-0.45	**0.015**	74465.34	53850.42
Ryr2	Ryanodine receptor 2	-0.42	**2.5E-05**	95617.29	71024.99

Table S9. Antibodies used for Immunohistochemistry and Western Blots.

Primary antibody target	Source	Experiment	Dilution
α-actinin	sigma A7811	IHF	1:20
Cmya5	abcam ab75351	IHF	1:25
Cmya5	NovusBio NBP1-77117	WB	1:1000
Collagen1	abcam ab6308	IHF	1:100
Collagen3	abcam ab7778	IHF	1:100
Dhpr	abcam ab58552	IHF	1:50
Dhpr	Alomone ACC-003	WB	1:500
GAPDH	Sigma PLA0302	WB	1:2000
Junctophilin-2	Santa-Cruz sc-377086	WB	1:1000
Obscurin	Atlas antibody HPA019497	IHF	1:100
Obscurin	Milipore ABT160	WB	1:1000
Ryr2	abclonal A0298	IHF WB	1:200 1:500
Serca2	Abclonal A1097	WB	1:1000
Synemin	Atlas antibody HPA040066	IHF WB	1:50 1:500
Titin is7	(Charton et al., 2016)	IHF WB	1:2 1:2000
Titin M8M9	Myomedix	IHF WB	1:75 1:2000
Titin M10	(Hackman et al., 2008)	IHF WB	1:75 1:2000
Titin Z1Z2	Abnova H00007273-M06	WB	1:2000

Table S10. Taqman probes used for qRT-PCR.

Gene	Taqman probe
Atp2a2	Mm01201431_m1
Cacna1c	Mm01188822_m1
Cmya5	Mm01282681.m1
Col1a1	Mm00801666_g1
Col3a1	Mm00802300_m1
Fn1	Mm01256744_m1
Jph2	Mm00517621_m1
Myh6	Mm00440359_m1
Myh7	Mm01319006_g1
Nppa	Mm01255747_g1
Obscn	Mm01341542_g1
Ryr2	Mm00465877_m1
Synm	Mm00809202_s1
TgfB1	Mm01178820_m1
Timp1	Mm01341361_m1
Ttn	Mm00621005_m1
Vim	Mm01333430_m1

REFERENCES

CHARTON, K., SUEL, L., HENRIQUES, S. F., MOUSSU, J. P., BOVOLENTA, M., TAILLEPIERRE, M., BECKER, C., LIPSON, K. & RICHARD, I. 2016. Exploiting the CRISPR/Cas9 system to study alternative splicing in vivo: application to titin. *Hum Mol Genet,* 25**,** 4518-4532.

HACKMAN, P., MARCHAND, S., SARPARANTA, J., VIHOLA, A., PENISSON-BESNIER, I., EYMARD, B., PARDAL-FERNANDEZ, J. M., HAMMOUDA EL, H., RICHARD, I., ILLA, I. & UDD, B. 2008. Truncating mutations in C-terminal titin may cause more severe tibial muscular dystrophy (TMD). *Neuromuscul Disord,* 18**,** 922-8.